applied sciences

MDPI

Article

Modelling of a SMA Blade Twist System Suited for Demonstration in Wind Tunnel and Whirl Tower Plants

Salvatore Ameduri [1,*], Monica Ciminello [1], Antonio Concilio [1], Ignazio Dimino [1], Bernardino Galasso [1], Mariano Guida [2], Giovanni Bruno [3] and Marco Fabio Miceli [4]

[1] Department of Adaptive Structures, The Italian Aerospace Research Centre (CIRA), 81043 Capua, Italy; m.ciminello@cira.it (M.C.); a.concilio@cira.it (A.C.); i.dimino@cira.it (I.D.); b.galasso@cira.it (B.G.)
[2] Department of Simulations and Virtual Reality Applications, The Italian Aerospace Research Centre (CIRA), 81043 Capua, Italy; m.guida@cira.it
[3] Laboratory of Space Qualification, The Italian Aerospace Research Centre (CIRA), 81043 Capua, Italy; g.bruno@cira.it
[4] ALI—Aerospace Laboratory for Innovative Components—S.C.A.R.L., 80146 Naples, Italy
* Correspondence: s.ameduri@cira.it

Featured Application: This work can find application in the field of the mitigation of the environmental impact of rotorcraft since it focuses on a system to reduce power consumption and, thus, pollution at specific flight regimes.

Abstract: In this work, the modeling of a demonstrator of a morphing system aimed at altering the twist of a rotorcraft blade is presented. The device was conceived for two different representative environments: the wind tunnel plant of the University of Bristol and the whirl tower facility of the DLR, for tests in fixed and wing rotary configurations, respectively. The concept, conceived and matured within the European Project of SABRE, is based on shape memory alloys, SMA. This technology was selected for its intrinsic compactness and solidity, which better meet the requirements of a typical blade structure, being extremely flexible and subjected to relevant inertial loads. A dedicated structural layout was conceived to favor the working modality of the SMA torsional system; this architecture was tailored both to absorb the typical actions occurring onto a blade and to assure a certain level of pre-twist necessary for the SMA strain recovery. The activation of the SMA was performed through an electrothermal helicoidal coil wrapped around it. A dedicated network of sensors was integrated within the structure to measure the impact of the different actions on the blade system. This subsystem, functional to shape reconstruction operations, is capable of splitting the contribution of the loads to pure twist and flapping. At first, the requirements imposed by the two test facilities were elaborated together to the operational needs, arriving at the issue of the most relevant specifications. Secondly, the conceptual and advanced design were considered, demonstrating, first, the feasibility of the concept and, then, its compliance with the test environment. The work ends with two different layouts, conceived respectively for the tests in fixed and rotary wing configurations. For both of them, a performance estimate was addressed, and a discussion on the advantages and disadvantages was presented.

Keywords: blade twist; SMA torsional actuation

check for updates

Citation: Ameduri, S.; Ciminello, M.; Concilio, A.; Dimino, I.; Galasso, B.; Guida, M.; Bruno, G.; Miceli, M.F. Modelling of a SMA Blade Twist System Suited for Demonstration in Wind Tunnel and Whirl Tower Plants. *Appl. Sci.* **2023**, *13*, 12039. https://doi.org/10.3390/app132112039

Academic Editor: Jérôme Morio

Received: 8 October 2023
Revised: 27 October 2023
Accepted: 30 October 2023
Published: 4 November 2023

Copyright: © 2023 by the authors. Licensee MDPI, Basel, Switzerland. This article is an open access article distributed under the terms and conditions of the Creative Commons Attribution (CC BY) license (https://creativecommons.org/licenses/by/4.0/).

1. Introduction

The aerospace industry is facing new challenges related to contingencies of different nature. Climate change, to cite an example, imposes, from one side, the adoption of a series of measures to mitigate the environmental impact of the aircraft and, from the other side, the development of dedicated strategies to deal with the arising weather instability [1]. To cite another example, the extreme competition within the aerospace compartment is a crucial aspect that can dramatically make the difference between the survival or extinction

of a market player. This situation is made even more critical by unpredictable events such as the COVID-19 pandemic, which led to a dramatic reduction of passenger-kilometers [2], or the Ukraine–Russia war that imposed longer and, thus, more expensive routes [3]. The policy, on one side, must define dedicated economic strategies and allocate funds for new programs, while the scientific community, on the other side, has to identify new approaches to the problems and develop novel technologies.

In this complex scenario, strategies focusing on both aircraft environmental impact and relevant costs are strategically important [4,5]. The concept of adaptation, that is to say, the capability of changing some features, can be exploited for those design cases not completely covered by the conventional approach [6]. Off-design conditions and flight segments penalized for their incompatibility with other extended ones are just some target applications for adaptivity. Wings for aircraft and main rotors for rotorcrafts can benefit from this approach [7,8]. In these cases, since the focus is mainly on the geometry change, one uses the word "morphing." This discipline is not so new. Starting from the world of nature up to the early days of aviation, it found several applications. Birds [9] and the flyer plane of the Wright brothers [10], in fact, embody the morphing wing concept. In the following decades of aviation, this approach was not abandoned but revisited to face growing loads [11]: the extremely flexible wing of the first aircraft gave way to more rigid versions equipped with movable parts. However, despite their capability of altering the load distribution, conventional flaps, slats, and ailerons for aircraft and swash plates for rotorcrafts alter the smoothness of the aerodynamic surfaces. Here, both the external kinematic chains needed for actuation and the geometrical discontinuities at the interface with the wing main body dramatically worsen the overall aerodynamic performance.

In the last decades, the advent of a new family of materials, namely "smart", changed the design perspective. To cite an example, active materials such as shape memory alloys, SMA, have been in the spotlight for their capability to bear loads and their relatively high force and power density. These peculiarities, in fact, make this type of material particularly suited for applications requiring large deformations and, at the same time, provide adequate flexibility to allow the morphing. In line with this trend, different programs were funded to mature morphable wing concepts and fill the gap for their industrialization [12]. Many programs in the last two decades were funded to comprehend the exact limitations of the morphing technology and the materials considered. Starting from the beginning of this century, the 5th European FP5-GROWTH Program funded the Project "Active aeroelastic aircraft structure" (3AS) to develop concepts able to alter wing mechanical features and achieve optimized configurations under the action of external loads [13,14]. The next Program, FP6, funded other projects focusing on the topic: the project of "Integration of technologies in support of a passenger and environmentally friendly helicopter" (FRIENDCOPTER), focusing on the estimate of the environmental impact of the rotorcraft and on the identification of some strategies of mitigation [15]. In the same program, the project "Smart High Lift Devices for Next Generation Wings" (SADE) [16] considered the development of high lift morphing systems characterized by a smooth geometry prone to the preservation of the laminar flow. In the next framework, the project "Smart Intelligent Aircraft Structures" (SARISTU) [17] addressed the problem of the integration of morphing devices within aircraft. Then, at the European level, Clean-Sky, a public-private partnership between the European Commission and the European aeronautic industry, was constituted [18]. Within this partnership and its extensions, Clean Sky 2 [19] and Clean Aviation [20], different projects were funded with the specific scope of maturing and demonstrating, in relevant environments, the most promising technologies to bring them in flight and pave the way towards industrialization. Among the different projects framed in these programs, one recalls: "JTI-Clean Sky 1-Green Regional Aircraft-Integrated Technology Demonstrator" [21], pointing to weight reduction, energy saving, and aerodynamic efficiency increase through break-through technologies as morphing wings; "AIRGREEN2" [22] focusing on the maturation and demonstration of laminar flow, high lift and load control, wing morphing, and turbulator strategies to mitigate the

environmental impact of the aircraft. Also, "Hybrid Electric Regional Wing Integration Novel Green Technologies" (HERWINGT) [23] fostered the decarbonization of aviation systems using new technologies as morphing.

Within this scenario and with a specific focus on blade morphing, the Program Horizon 2020 funded SABRE's research project: "Shape Adaptive Blades for Rotorcraft Efficiency" (2017–2021) [24]. The ambition of this project was to mitigate the environmental impact of the rotorcraft, implementing innovative morphing architectures on the main rotor of the Bo105 rotorcraft, predicting their impact through dedicated tools, and finally demonstrating them in a representative environment, such as a wind tunnel and whirl tower. The developed concepts involved the adaptive variation of twist [25], chord, and curvature [26–28]. Still, within the same theme, Bell Helicopter presented, at the Heli-Expo in Dallas in 2017, the FCX-001 aircraft, including, among others, innovative systems for blade morphing, highlighting the growing interest of the aerospace industry in the topic [29]. Still speaking of research programs and some years before, in 2009, within the DARPA research program, NASA demonstrated the possibility of reducing hub noise and vibration in relevant environments through advanced adaptive systems based on smart materials [30]. The growing interest in blade morphing is also evidenced by the number of scientific publications on its use in the blades of highly integrated actuation architectures. Among the most recent ones are the study of SMA-based skins for blade chamber variation [31], the strength analysis of the blade region for the later integration of an SMA actuator [32], and the active vibration control of rotating blades using piezoelectric actuators [33]. Still on the blade morphing topic, but with a focus on renewable energy production, one recalls INWIND "Innovative Wind Conversion Systems (10–20 MW) For Offshore Applications" (2012–2017), funded within the 7th Framework program and targeting the conceptual design and development of innovative off-shore concepts and their demonstration [34]. These systems proved their capability to reduce the levelized cost of energy dramatically. Another example in the sector is the project "Morphing Blades: New-Concept Tidal Turbine Blades for Unsteady Load Mitigation", funded by the Engineering and Physical Sciences Research Council and focusing on the demonstration, at a scale level, of innovative systems able to mitigate the unsteady loading of tidal turbines and reduce their levelized cost of energy [35,36].

The present work focuses on the part of the activities addressed by the Italian Aerospace Research Centre, CIRA, within the above-mentioned SABRE project. CIRA developed a blade morphing system belonging to the family of compliant architectures capable of producing an adaptive twist using compact and solid actuators based on SMA technology. The adaptive twist offers advantages in terms of [37]:

- Reduction in the power required by the main rotor and improvement in its performance; in refs. [38,39], a reduction in power between 5 and 15% was estimated by implementing the adaptive twist in synergy with other morphing strategies. This dramatically mitigates the environmental impact of the rotorcraft, with a net reduction of NO_x emissions of about 5–8%;
- Improvement of the maneuverability at different flight regimes; this aspect, as discussed in ref. [40], directly derives from the capability of reducing the power consumption and optimizing the load distribution on the blade;
- Abatement of noise and vibrations up to 65%, as discussed in refs. [41,42];
- Enhancement of the safety and stability of the rotorcraft in case of failure and gust. This aspect is strictly related to the better distribution of the loads on the blade, obtainable by altering the twist, and to the mitigation of vibration at the hub.

Despite these noteworthy advantages, some relevant challenges have to be outlined; among the others:

- The cross-section of the blade is generally characterized by a small area integrated with a cell-like structure covering the leading-edge zone up to the maximum thickness of the airfoil [43]; this architecture is suited to increase the stiffness but represents an obstacle for the implementation of potential morphing architectures, as a droop

nose or the twist itself. Even the aft part of the airfoil is stiffened by the skin and a hard foam or honeycomb that should be accurately considered before implementing a chamber morphing.

- The just mentioned narrow space dramatically limits the use of the actuators: solutions characterized by compactness and high power and force densities play, in this case, a crucial role. Also, the flexibility of the blade and the centrifugal forces represent a challenge for the actuation. The large displacements of the blade due to the inertial forces determine the relative movement between the internal parts of the actuators, favoring friction and, thus, loss of actuation or, in the worst case, jamming. SMA elements, in the case of steady applications, can be considered for this type of actuation, even if their non-linearity, fatigue behavior, and performance should be carefully considered because of their dependence on the cycles of activation.
- The implementation of morphing cannot be separated by the development and integration of dedicated logic and sensor networks. It is important for structural health monitoring and for shape reconstruction purposes that the logic can determine the level of solicitation of the structure, separating the contribution of twist and bending in the flap and lag directions from that due to inertial, aerodynamic, and internal actuation. The sensor layout has to be accurately investigated to adequately support the logic and fit the best narrow space; moreover, the sensors should withstand the harsh environment represented by the large displacements and the centrifugal actions.

The scope of the architecture ideated by CIRA is to improve the performance of the rotorcraft for some specific flight regimes, such as hover and vertical flight. These regimes are generally penalized by the conventional design due to their requirements, which are in conflict with more extended regimes. The structural design needs to consider requirements of a different nature: first, the safety in terms of structural integrity and thermal and electrical protections during test execution; second, the achievement of the prescribed morphed (twisted) shape under the most severe load condition; third, the exploitability of the measurements.

After having illustrated these requirements and their impact on specific features of the model, the work focuses on the conceptual and advanced design, highlighting the differences between the two test/working configurations investigated, that is to say, the fixed and rotary wing for wind tunnel and whirl tower tests.

On the basis of the outcomes of the modeling task, a critical comparison is finally tracked between the specifications and the predicted performance of the architecture.

2. Specifications

The architecture presented in the next part of the work was conceived to produce an additional pitch-ward twist on a blade segment in a steady state condition, independently from the azimuthal position of the blade. The rotor of the Bo105 was assumed as a reference. The required additional twist must follow a linear trend along the span, achieving a maximum pitch-ward of 8 deg at the tip on a span of 5 m and considering a useful distance between 20 and 90% of the radius, which means an additional twist gradient of 2.3 deg/m. This twist meets the necessity of getting an induced drag as uniform as possible along the span to increase the figure of merit [44]. This approach is effective for hover conditions, and conventional blades are manufactured with an original twist, tending to reduce the lift at the tip because the flow pattern makes more uniform the induced drag. This has a relevant impact on the figure of merit, which may be increased by 5%, with a net rise of up to 20% of the payload [44]. However, conventional twist laws are limited by the undesired impact that they could have in forward flight. Here, the back-and-forth excursion of the center of lift of the disc rotor against the azimuthal rotation of the blade makes difficult the achievement of a trimmed condition [44]. Investigations on the specific architecture proved a reduced needed power of about 10% in hover and some benefit, 2% on average, up to a forward speed of 30 m/s [45].

Other important aspects drove the assessment of the final layout: first, the narrow room within the blade to host an actuation system; second, the flexibility of the structure that undergoes large displacements; third, the magnitude of the centrifugal actions. The narrow space led to the consideration of compact actuation solutions characterized by high energy densities. Friction among contiguous parts, gaps, and free-play angles, which is problematic in terms of loss of effectiveness, made the designers converge towards solid, monolithic solutions. SMA materials seemed a good candidate for the application, also offering adequate stiffness and, thus, being able to absorb loads together with the pre-existing blade structure.

However, the use of an SMA actuator, even for a prototype, poses some specific issues. Achievable performance, differently from conventional actuation, depends on the level of prestress. In practice, a certain pre-load (in the specific case, pre-twist) must be provided to enforce the transformation of the austenite phase into martensite. In fact, the more martensite is initially present, and the more austenite can be potentially produced by heating the material, with the macroscopic effect of larger displacement recovery. The drawback is that the structure hosting the SMA will have to bear conventional loads (aerodynamics, inertial) plus the ones due to the pre-twist of the SMA actuator. Another critical aspect is the thermal management. The temperature of activation of the SMA must be, in fact, adequately higher than the maximum level foreseen by the flight envelope of the rotorcraft to avoid undesired activation. This poses a number of problems: the protection of the structural and electronic components from the heat source, the control of the temperature level involving dedicated sensing and logic, and the effectiveness of heating, which must minimize losses and guarantee a uniform temperature within the SMA material. Finally, last but not least, the de-activation performance is a cooling time that is adequately short to fit operational requirements.

In addition to the requirements discussed above, there are others strictly related to the demonstration in the wind tunnel and whirl tower plants. First, the structural integrity imposes a safety factor greater than 2 on all the parts of the main structure. This limitation was not applied to the SMA being pre-loaded for activation purposes; however, to mitigate any risk, the SMA was hosted within the main structure, avoiding any fragment projection. The second requirement is the maximum temperature the SMA can reach during the tests; for safety reasons and also considering the scarce heat transfer due to the hosting, a maximum heating temperature of 180 °C was allowed, and dedicated safety fuses were considered within the power supply circuit. Third, the mass distribution for stability reasons was kept within the 1st quarter of the chord. Then the test velocities: the maximum speeds, 25 m/s and 120 rpm, considered for the WT and WhT experimental campaign are well below the limitations of the facilities, at 50 m/s and 1200 rpm. Moreover, the relevant loads are also lower than the ones due to a blade nominal speed of 44.4 rad/s (=424 rpm). The selected maximum speeds, however, are, from one side, representative of portions of the blade closer to the axis of rotation and, from the other side, give a trend of the impact of the loads on the functionality of the actuation system and the stress level and performance [46].

Other requirements involve the measures. Three types of measurements must be performed through onboard sensors: temperature of the SMAs, inclination around the span and the flapping axes, and strain at specific regions in view of the future assessment of shape reconstruction logic. The temperature is measured by K-type thermo-couples integrated into the heaters; the measurement range of this type of sensor ($\geq$400 °C) is much higher than the allowed maximum temperature of 170 °C. The measurement range of the inclinometer must be compliant with the expected twist and flapping rotations; an interval wider than $\pm$20 deg and an accuracy lower than 0.1 deg was considered appropriate against the prescribed actuated twist over the entire blade segment and on a single bay. Finally, a minimum detectable deformation of 5 $\mu\varepsilon$ and a measurement range of 2000 $\mu\varepsilon$ were assumed for the strain sensors. The compliance of these values with the need to measure the twist with an accuracy of 0.1 deg and the allowed maximum stress level will be discussed

in the section dedicated to the modeling. For sake of clearness, the above-mentioned requirements were reported in Table 1.

Table 1. Requirements of the blade twist prototypes.

Parameter	Value	Impact	Notes
Additional twist	≥8 deg/R, pitchward	Performance	This requirement was determined using investigations on the main rotor of the Bo105.
Cross section	Shape: NACA23012 Chord: 267 mm	Aerodynamic performance	This parameter comes from the reference rotorcraft, the Bo105.
Activation temperature of the SMA	≥90 °C	Power consumption Subsystems thermal protection	The lower limit of this parameter was set to avoid undesired activations caused by high environmental temperatures. Given a maximum environmental temperature of 25 °C for the tests planned in the project, this limit was fixed in view of future flight demonstrations, characterized by operational temperatures in the range of [−50, +80] °C.
Maximum temperature of the heating source	≤180 °C	Power consumption Subsystems thermal protection	This limitation is strictly related to tighter safety requirements because the source used to heat the SMA is hosted within the blade, with modest heat transfer capabilities.
Power supply	≤600 W	Power consumption	This parameter is driven by the test plants.
Safety factor for all structural parts of the blade (SMA excluded)	≥2	Structural integrity	This requirement comes from the test facility's safety restrictions.
Allowable stress in the SMA	≤700 MPa	Structural integrity	The high level of allowable stress is strictly related to the necessity of generating enough martensite phase during the pre-load task. This value does not take into account fatigue problems since the present application was conceived for WT and WhT tests.
Mass distribution	Center of gravity within the 1st quarter of the chord	Stability	This constraint is linked to the stability requirement, especially for rotary tests.
WT speed	≤25 m/s	Structural integrity	The speed limitations are strictly related to the above requirement for a safety factor greater than 2. Although these values lead to lower loading conditions than the nominal one occurring at a speed of 44.4 rad/s, they allow us to appreciate the trend of the impact of aerodynamic and inertial loads on the structural integrity and actuation functionality.
WhT speed	≤120 rpm	Structural integrity	
Thermocouple sensor	Maximum temperature ≥ 400 °C	Safety Level of activation	The maximum detectable temperature is well over the maximum expected temperature of 180 °C.
Inclinometer measurement range and accuracy	Range no smaller than [−45,+45] deg accuracy ≤0.1 deg	Performance measurement	The measurement range is compliant with expected twist and flapping rotations well below +/−20 deg. The accuracy limit is about 1 order lower than the minimum twist expected by each bay (1 deg).
Strain sensor measurement range and accuracy	Range within [−2000,+2000] με Minimum strain (absolute value) ≥ 5 με	Pre-load, twist measurement	The measurement range and the minimum strain detectable will be discussed in the modeling section against the twist produced by the preload and the most severe load condition.
Cabling and routing	All the cabling must exit from one edge of the demonstrator	Logistic	This requirement is strictly related to the interfaces of the test facilities that allow the cable to pass only through one edge of the prototypes.

3. Working Principle of the Concept and Main Features

The architecture is made of different cell elements serially connected along the span. Figure 1 shows, on the top, two cells connected to each other, one covered by the skin and the other naked. The main parts of a cell are:

- The main structure: this is a solid element made of aluminum alloy; two lateral blocks reproduce the leading edge shape; one of them presents a square hole, while the other one has a lateral circular opening and four radial holes. The blocks are linked by two transversal spar elements whose shape was set to minimize the stress due to the external loads and to transmit the twist; holes were made in the aft spar; these were used to pass through the supply cable for the heating coil, and a thermocouple was used to measure the temperature of the SMA (see detail on the scheme on the left of Figure 1).
- A pre-twisted SMA rod actuator is mounted in the main structure between the two spars; one edge is clamped into a side block.
- A heating coil is wrapped around the SMA rod; when required, this thermo electrical component is switched on to increase the temperature of the alloy and enforce phase transformation, with the macroscopic effect of recovering angular strain.
- A ring-like element made of steel alloy (see detail on the scheme on the right of Figure 1), where the element is fixed on the other edge of the SMA rod. The side face of the ring is suitably shaped to apply a torsion through a dedicated tool, while the outer cylindrical surface presents four radial holes. During the pre-twist operation, these holes are aligned to the corresponding ones on the main block and finally filled in by pins to avoid any relative rotation between the parts.
- A couple of truss-like elements made of aluminum alloy reproducing the lateral ribs. These elements are connected to the main structure and transmit the twist to the external skin.
- A plate element between the two ribs at the trailing edge zone, made of aluminum alloy, integrated with strain sensors. This element is clamped at one rib and can slide within the opposite one; external actions are transmitted by the lateral ribs to the plate; the twist and/or the bending of the cell are then estimated through a dedicated logic that elaborates the strain measures. FBG fiber optic sensors were selected after a trade-off among different strain sensors: resistive strain gages, piezoceramics, and fiber optics. Piezoelectrics are characterized by a wider operational frequency band and a higher sensitivity compared to the other types of sensors considered. Their fragility and, above all, the routing of the connections within the blade narrow space, however, discouraged their use. The same cabling issue limited the use of resistive strain gages, adopted for comparison in tests in the wind tunnel and in substitution of the FBGs during the whirl tower campaign in compliance with specific requirements of the interface of the facility. On the contrary, fiberoptics improved, offering the attractive possibility of accommodating more FBG onto a unique line. Epoxy resin was used to finalize the bonding on the plate's metallic surface.
- An inclinometer sensor mounted on a supporting plate is used as a reference for the estimate performed through the strain sensors installed on the plate element. The use of this type of sensor was considered for verification purposes. As clarified below, the strain information provided by the fiberoptics will be elaborated by a dedicated logic of shape reconstruction to get a view of the blade's current configuration. In line with this, the inclination around the three axes will be used to tune the system for assigned types of solicitations and validate the logic of reconstruction under the combined action of different loads.
- A couple of masses are made of lead: these masses, with the same shape as the leading edge, are mounted on the main structure's lateral blocks and contribute to keeping the center of gravity in the first quarter of the chord.

- The skin is screwed to the rib elements and to the main structure; it contributes to keeping the aerodynamic shape under the external loads and the twist action of the actuator.

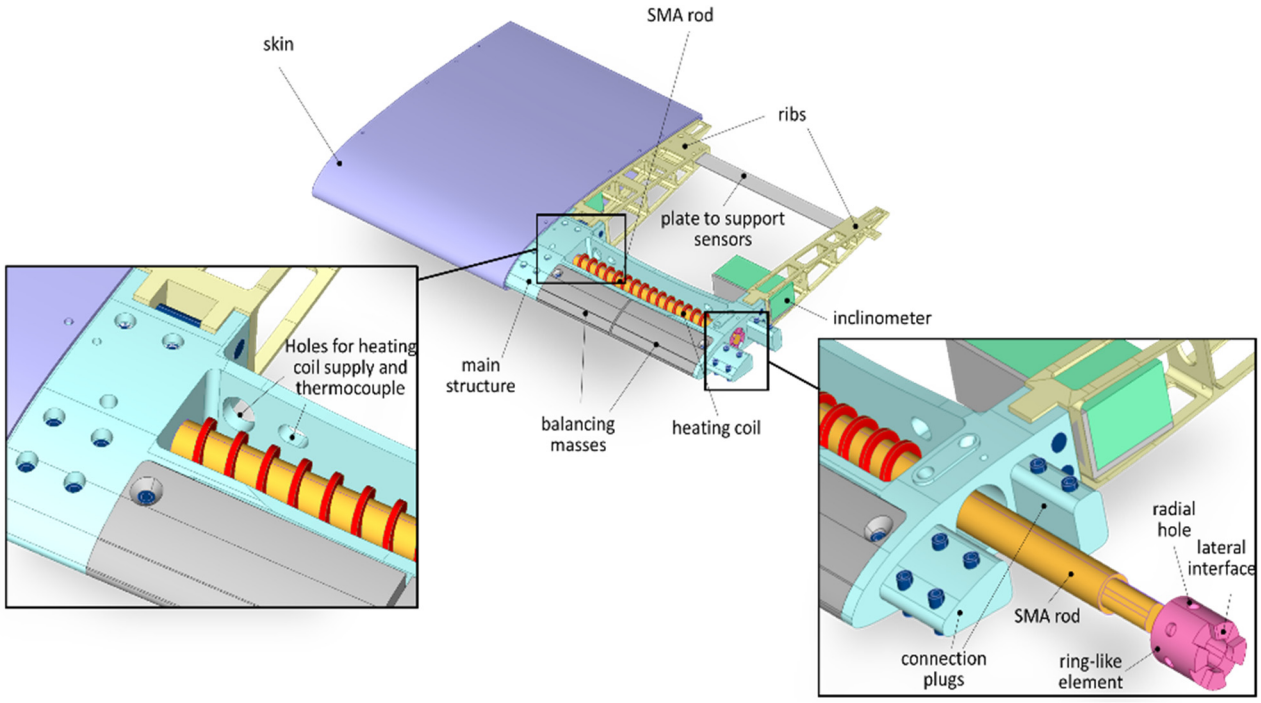


Figure 1. Layout of the device: two cells connected (**top**); detail of the holes within the spar for heating coil supply and the thermocouple (**left**); detail of the ring-like element (**right**).

SMA torsional actuators obtained the actuation. The simplicity of the transmission and the possibility of minimizing the number of parts led to the consideration of torsional active elements rather than other shapes and types of actuation (wires, ribbons transmitting axial forces) [47]. Rods and tubes were both candidates. The centrifugation of the areas of a tube assures a higher bending and torque stiffness over mass ratio compared to a rod of the same diameter. The inner cavity, moreover, can be exploited as an inlet for cold air for the refrigeration and the de-activation of the alloy. Furthermore, the pre-twist of an SMA rod cannot produce martensite in the inner core since the stress level does not grow enough, as will be discussed in the next part of this section. This results in a portion of material that cannot be exploited for actuation and must be twisted together with the structure without contributing to the overall stiffness. However, some drawbacks of the tube layout led the designers to consider the rod. First, the structural instability of the wall under the combined action of the pre-twist and the bending and torque coming from conventional loads. Second, the magnitude of the torsion to be applied to the pre-twist tube is relatively higher because of the higher inertia moment. Thus, considering the target TRL of the prototypes [48], conceived for demonstration in facilities with relevant safety factor restrictions, the designers chose the rod shape. The selection of the material was dictated by the elastic properties, the recoverable strain, and the temperatures of activation. These parameters have a relevant impact on transmitted twist, power consumption, and thermal safety. Another not negligible aspect that drove the choice was the availability of products with the required size on the market. The market offers a wide variety of SMA products, usually of relatively small size and derived from wires and sheets. Rod elements are difficult to find since they require dedicated tooling, and the machining forces may alter the microcrystalline composition. Based on a survey of the worldwide market, it was possible to find rod elements of a diameter greater than 8 mm made of NiTiNol alloy with transition temperatures compatible with the requirements.

It is worth clarifying a fundamental aspect before illustrating the design approach adopted for the SMA actuators. As already specified, the capability of these alloys to recover strain is strictly related to the transformation of the martensite phase into austenite, obtained by heating. In this sense, the presence of the martensite phase plays a critical role. In fact, the higher the initial martensite percentage, the higher the strain that can be potentially recovered. A certain stress level must be assured to produce an adequate amount of martensite. For this reason, the SMA elements are pre-twisted and mounted onto the structure. Then, they are released to achieve the elastic equilibrium with the structure. The residual stress thus determines the level of martensite.

The approach adopted for the definition of the features of the actuator is based on the conceptual scheme illustrated in [47]. The SMA element is initially seen as a 1D actuator, considering only the torsional dof. The element is clamped at one side, and a twist is applied at the other edge. This produces a linear, angular strain along the radius at each cross-section of the SMA element. The corresponding shear distribution is computed using the theoretical model described in ref. [49]. In line with the 1D assumption, both strain and shear do not depend on the tangential or axial coordinates but only on the radius. When the SMA rod is twisted, the three different situations shown in Figure 2 may occur [50]: in case (a), the applied twist is not enough to produce phase transformation, and no activation can be obtained by heating. Meanwhile, in case (b), the twist is higher, and a ring region of phase transition appears; only a partial activation can be obtained. Finally, in case (c), the level of twist (and thus the stress generated) is sufficient to produce an outer martensite region, fully exploitable for activation. The scope of the design is to generate as much martensite phase as possible; this will be transformed into austenite by heating, with the macroscopic effect of recovering strain.

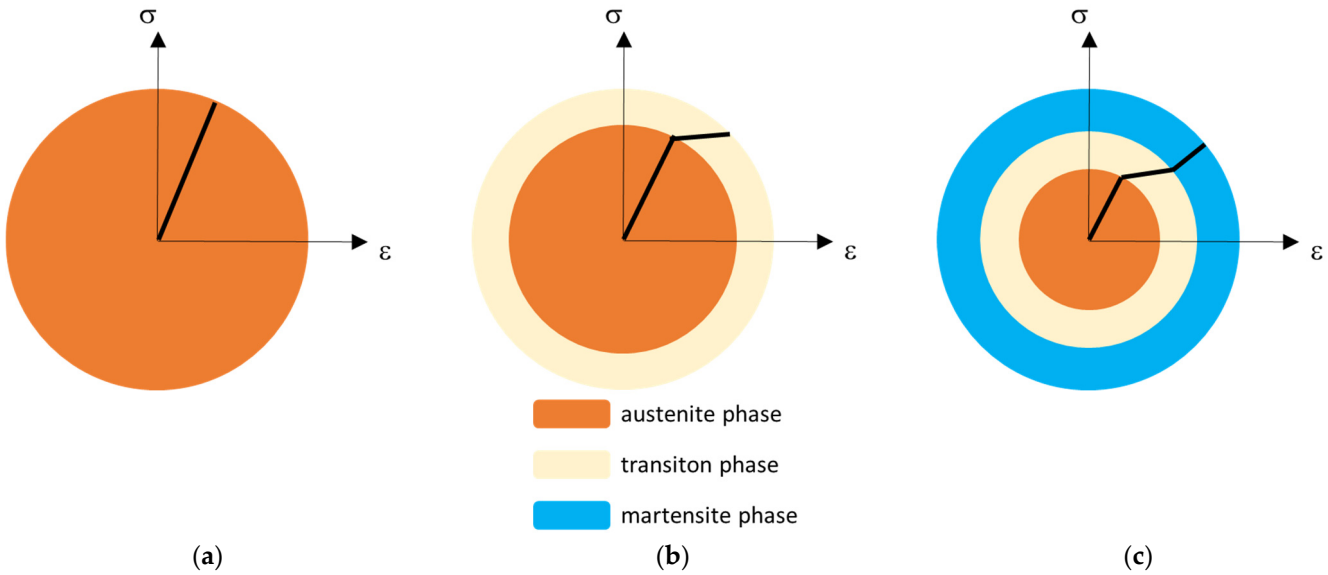


Figure 2. Stress-strain distribution in the cross-section of a SMA element: full austenite (**a**), austenite core plus transition phase (**b**), austenite, transition phase, martensite (**c**).

The momentum of the shear acting on each elemental ring is then computed with respect to the axis of the rod. Finally, it is integrated towards the entire radius to get the torsional moment. This process is repeated for twist angles ranging between 0 and 90 deg and for values of temperature between 25 and 200 °C. In this way, all required load-unload torque-twist curves can be built.

At this point, the torsional rigidity of the blade structure is computed. This operation, in line with the preliminary level of the design, is addressed considering the geometrical parameters and inertia moments of the cross-section. This allows us to draw the equivalent torsional elastic line of the structure.

The last step of the procedure consists of preparing a plot to compare the load-unload torque twist curves and the just-mentioned elastic line. In Figure 3, a qualitative representation of this graph is shown. The load-unload cycles of the SMA at four different temperatures ($RT < T_1 < T_2 < T_3$) were plotted. All the cycles arrive at the same maximum angle of twist. At each temperature but the highest one, T_3, phase transformation occurs, as indicated by the hysteretic behavior. However, the areas of the cycles become less and less pronounced as the temperature rises up to collapse to the red straight line at $T = T_3$. This condition corresponds to case (a) of Figure 2, for which the stress achieved within the twist range is not enough to allow any phase transformation, and the rod remains in pure austenite.

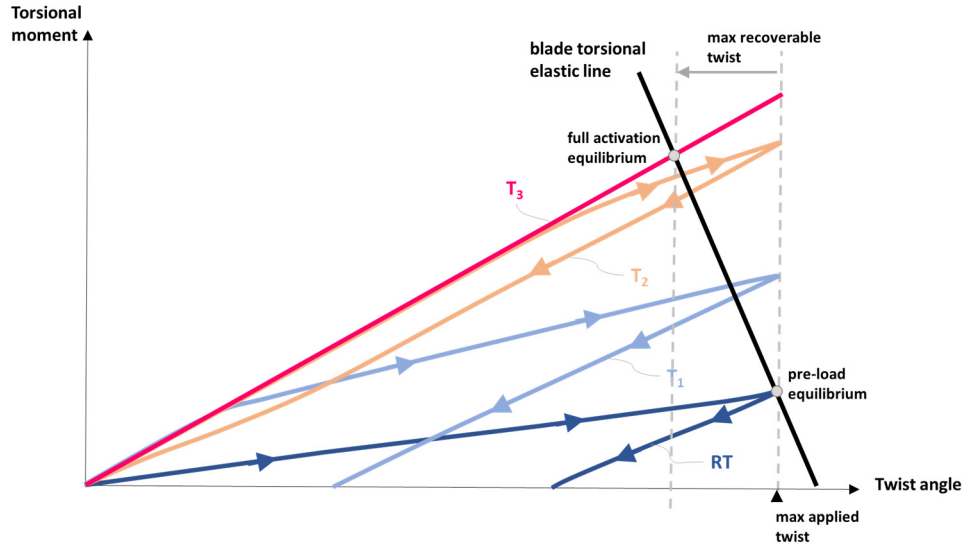


Figure 3. Comparison plot between the blade equivalent torsion elastic line and the load-unload torsional cycles of the SMA at different temperatures.

The "pre-load equilibrium" point represents the equilibrium condition in pre-twist at RT, between the blade and the SMA. As the temperature rises, this point moves upward and leftward on the cycles at higher temperatures to arrive at the "full activation equilibrium" on the straight line ($T = T_3$). The horizontal distance between the pre-load and the full activation points represents the maximum recoverable twist.

This simplified scheme was used to address the preliminary identification of the main features of the SMA actuators, whose complex behavior was investigated through the refined FE models described in the next section.

The mentioned SMA components can be heated essentially in two ways: by energy production (Joule effect) and external supply (conduction, convection, irradiation). The first approach is generally preferred for small sizes (wires, ribbons) since the required current is relatively low (<10 A). However, as the cross-section grows, this value becomes prohibitive. Furthermore, to avoid short circuits, the SMA must be adequately insulated from the other conductive parts, but this operation is often difficult to reconcile with the need for a mechanical transmission that requires a strong connection. Due to the diameter of the SMA rod selected for this application (10 mm), the option of the external energy supply was chosen. The external surface of each SMA rod, except the zones clamped within the main block (180 mm over a total length of 220 mm), was covered by the heating coil, as shown in Figure 1. A total of 16 turns were used per SMA, spaced between each other to guarantee a uniform distribution of the temperature along the rod axis and compensating conduction losses occurring at the clamped edges. A 5 × 3 mm rectangular cross-section was selected for the coil curb to guarantee an effective flat contact with the SMA surface.

The process identified for the preload can be summarized in the following steps:

1. With reference to Figure 1, the main structure is clamped on the left side; this operation is performed through a bench vise.
2. The heating coil is placed between the two spars and centered with respect to the lateral holes present on the two sides of the main structure.
3. The SMA rod is inserted into the main structure, passing through the circular hole illustrated in the bottom right detail of Figure 1 and, then, through the heating coil; the operation ends with the embedding of the square milled left edge of the SMA rod into the shaped hole present in the left side of the main structure. As a result, the SMA rod is clamped on the left edge of the main structure.
4. The crown component is integrated on the SMA-free edge on the right and hosted within the circular hole. Note that the crown component presents a shaped hole suited to embed the edge of the SMA rod. The lateral interface is now completely inserted in the main structure.
5. A torsion couple is applied through a tailored tool, fitting the lateral interface of the crown illustrated in the bottom right detail of Figure 1. This operation lasts to achieve the alignment of the radial holes of the crown with the corresponding ones on the main structure.
6. Pins are inserted in the holes of the main structure to match the corresponding radial holes of the crown; as a result, the SMA-crown assembly is definitely constrained to the main structure.
7. The torsion couple is removed, letting the main structure and the SMA achieve the equilibrium.

The process described above is monitored through a dedicated sensor network to avoid exceeding the stress threshold and acquire the pre-load twist obtained. To this scope, the above-mentioned strain sensors were used. The integration process of these sensors was addressed after having joined all the cells along the span direction and before the installation of the skin. For both demonstrators, a unique interface through which driving cabling was identified. This is represented by the lateral cross-section suited for the connection to the whirl tower hub and to the actuator used to change the AoA during the tests in the wind tunnel. The cables relevant to the sensors of a certain cell are separated by the bundle and redirected to specific parts of the cell, while the remaining ones pass through the subsequent ribs to enter the next cell. A bonding process through an epoxy resin curing at RT was adopted for the integration of the strain sensors.

Following this approach, a specific layout was defined on a structural part, an aluminum alloy plate, clamped at one rib of the bay and sliding into a guideway within the opposite rib. Figure 4 illustrates the concept at the basis of the sensing network. Pure twists and pure bending between two consecutive ribs can be detected, as well as a combination of them. When, as during the pre-load process, pure bending is transferred on the plate (scheme (a)), bending and twisting are generated. The bending is detected by the sensors at the edges of the plate, placed in a collocated configuration, while only the twist is detected in the middle due to the inversion of the bending moment towards the plate span. When flapping solicitation occurs (scheme (b)), bending is detected both on the edges of the plate and in the middle. To correlate the strain measures with the plate deflection, an inclinometer was foreseen on each cell to detect the relative rotation around the chord and twist axes. Different types of inclinometers were considered, having as a constraint the range of measure, the accuracy, and the overall dimensions. The IS40 two-axial inclinometer was selected for this purpose, fitting the requirements in terms of the range of measure and accuracy in a compact volume of 60 $\times$ 30 $\times$ 20 mm [51]. Another important feature of this sensor is represented by the high shock resistance of 30 g, making it particularly suited to the harsh WhT environment.

Although the sensor network design is out of this work's scope, the strain caused during the operational tests was estimated in the next section to develop an idea of the expected sensitivity.

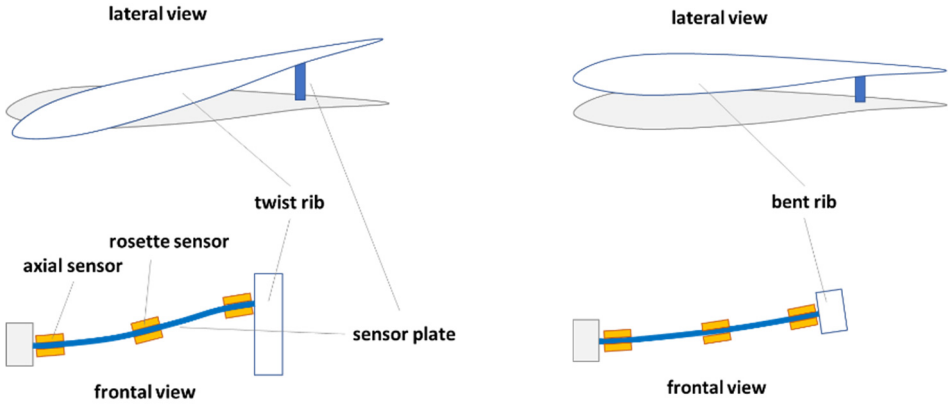


Figure 4. Sensor plate working principle: pure twist (**a**) and pure bending (**b**).

After having considered the interior parts, the skin was investigated. It has to meet different requirements. First, it must withstand the most severe load conditions, determined by the combination of the SMA transmitted twist and the different forces occurring during WT (aerodynamic) and WhT tests (aerodynamic + centrifugal). Second, it has to maintain the prescribed aerodynamic shape to guarantee acceptable performance of the system. Third, it must be flexible enough to permit the morphing twist. Different types of materials were considered during the preliminary design: aluminum alloy, glass and carbon fiber laminates, and plastic materials. Metallic and especially composite skins represent an optimal solution for conventional applications, assuring a flexibility level adequate for the load application scenario but not enough for a morphing application that would be thus penalized. Moreover, reduction of the thickness of the sheet to mitigate these losses would have been prone to instability events. Thus, attention was paid to a family of plastic materials with relatively high mechanical properties. It is worth noting that also the manufacturing process drove the choice of the material. In fact, to mitigate any surface discontinuity, a glove-like skin solution was taken into account. Additive manufacturing was exploited to this purpose. Two materials were considered: the ULTEM™ 9085 Resin [52] and the ALFANYLON CF [53]. Due to the higher heat temperature deflection, the former of these materials was finally selected for the realization of a 1.8 mm thick skin.

The logic of control is aimed at guaranteeing the achievement of the target temperature and maintaining it within an acceptable range of $+/-5$ °C. This choice and relevant tolerance derive, first, from safety considerations. The heating coil, in fact, is included in the cell between the two spars shown in the scheme on the left of Figure 1 and between the top and bottom parts of the skin, the most critical element from the thermal point of view. The maximum allowable temperature of 180 °C and the imposed tolerance are well compliant with the heat temperature of deflection of the ULTEM material (215 °C). However, to take into account, even any fault event of the logic, current, and temperature fuses were included in the supply circuit. Another important aspect concurring in the definition of allowed tolerance is strictly related to the impact that this deviation could have on the transmitted twist. As will be shown in the next section, this impact is negligible.

The information provided by the sensors is supposed to be collected and elaborated using dedicated equipment. In line with the main scope of the WT tests, that is to say, to estimate the impact of the twist on the aerodynamic performance, the onboard sensors have to provide information useful for the reconstruction of the current shape, which in turn is related to the aerodynamic measures. In this sense, a dedicated optical interrogator and a multi-purpose acquisition system will be necessary. This second piece of equipment will collect the information coming from the resistive strain gages, the inclinometers, and the thermocouples, assuring their synchronization. This aspect plays a critical role in the reconstruction of the behavior of the system in transient conditions; that is, after having

achieved stable conditions for the environmental parameters (speed, pressure), the SMA is activated to achieve the target configuration. The same equipment, except for the optical interrogator, is compliant with the WhT test campaign. Here, the scope is to relate the current configuration of the blade to the external loads; in this way, the capability of the system to correctly work under representative loads can be demonstrated. However, two aspects relevant to the noise of the measures must be accurately considered: first, the impact of the accelerations, especially during transient situations, and second, the presence of sliding contact in the sensor supply line. Off-line filtering operations are considered to improve the quality of the test outcomes.

Finally, for clarity, all the parameters considered in the next section for modeling are summarized in the following tables (Tables 2–8).

Table 2. Single bay features.

Feature	Value
Span length of the single bay	220 mm
Chord length	270 mm
Airfoil	NACA 23012
Main block material	7075-T6 aluminum alloy [54] (see properties in Table 3)
SMA material	NiTiNol (see properties in Table 4)
SMA rod actuator total length	222 mm
SMA rod actuator working length	180 mm
SMA rod diameter	10 mm
Crown connection between the main block and the SMA rod	15–5 PH steel alloy [55] (see properties in Table 5)
Heating coil	1 per bay with embedded thermocouple
Heating coil maximum achievable temperature	750 °C
Rib material	7075-T6 aluminum alloy
Skin material	ULTEM
Skin thickness	1.8 mm
Inclinometer	1 per bay, model

Table 3. 7075-T6 aluminum alloy features.

Feature	Value
Elastic modulus	71.7 GPa
Poisson ratio	0.33
Tensile yield strength	503 MPa
Ultimate tensile strength	572 MPa
Thermal conductivity	130 W/m°K
Specific heat	960 J/kg°K
Density	2810 kg/m^3

Table 4. SMA material features.

Feature	Value
Material composition	NiTinol alloy (55.79% of Ni, 0.11% of C, O, Cu, Fe, Co, Cr, Nb, H, N, balance Ti)
Elastic modulus in austenite and martensite phases	25 and 15 GPa
Poisson ratio in austenite and martensite phases	0.33
Martensite start and finish transformation stresses at 25 °C	150 and 325 MPa
Austenite start and finish transformation stresses at 25 °C	175 and 45 MPa

Table 4. *Cont.*

Feature	Value
Stress temperature gradient in forward and rearward transformation	6.8 and 7.6 MPa/°C
Thermal conductivity in austenite and martensite phases	18 and 8.6 W/m°K
Specific heat	836 J/kg°K
Density	6500 kg/m^3
Maximum recoverable strain	0.023

Table 5. 15-5PH stainless steel alloy features.

Feature	Value
Elastic modulus	210.0 GPa
Poisson ratio	0.33
Tensile yield strength	1172 MPa
Ultimate tensile strength	1310 MPa
Thermal conductivity	135 W/m°K
Specific heat	100 J/kg°K
Density	7800 kg/m^3

Table 6. Skin material, ULTEM 9865 TM, main features.

Feature	Value
Material	Polyetherimide (PEI)
Density	1.27 g/cm^3
Tensile strength	100 MPa
Tensile modulus	2700 MPa
Flexural strength	170 MPa
Flexural modulus	2800 MPa
Impact strength	78 J/m
Heat deflection temperature	215 °C
Glass transition temperature	220 °C
Flammability rating	UL94 V-0
Chemical resistance	Excellent resistance to a wide range of chemicals, including acids, bases, solvents, and fuels
Sterilization resistance	Can be sterilized using steam, ethylene oxide, or gamma radiation

Table 7. Whirl tower demonstrator.

Feature	Value
Number of bays	3
Total length (flange connection excluded)	660 mm
Connection flange material	15–5 PH steel alloy
Connection pins material	15–5 PH steel alloy
Balancing masses	6 (2 per bay)
Strain gages installed onto the supporting plate	18 (3 per side of each plate)
Tip flange material	ULTEM
Inclinometers	5 inclinometers (1 per bay counted in Table 2) + one at the root as reference
LED	2 LEDs installed at the tip, on the leading and trailing edge

Table 8. Wind tunnel demonstrator.

Feature	Value
Number of bays	4
Total length (flange connection excluded)	880 mm
Connection flanges	2, one per side of the demonstrator
Connection flanges material	15–5 PH steel alloy
Connection pins material	15–5 PH steel alloy
Balancing masses	8 (2 per bay)
Strain gages installed onto the supporting plate	24 (3 per side of each plate)
Fiber grating sensors	24 (3 per side of each plate)
Inclinometers	4 inclinometers (1 per bay counted in Table 2) + one at the root as reference

4. Modelling Approach

The advanced design was addressed by means of a dedicated finite element model. In compliance with the architecture of the real prototype, the model was structured in different cells independent of each other for activation and were connected along the span. Two versions, made of 3 and 4 cells, were considered, representing the prototypes for the whirl tower and wind tunnel facilities, respectively. Different constraint conditions were implemented. The model for the whirl tower was clamped at one edge, namely the root, and left free on the other edge. Differently, the model for the wind tunnel was clamped at one edge while all linear and angular dofs of the other edge were locked, except the ones along the span direction. This configuration was chosen to reproduce the mounting asset in the wind tunnel test room, which foresees one edge of the model clamped onto a motorized shaft for setting the AoA and the other edge hosted within the opposite wall of the test room and free of rotation to avoid any obstacle to the SMA twisting action. In Figure 5, the blade segment was represented as a beam, with the just mentioned constraint conditions.



Figure 5. Constraint conditions simulated for the whirl tower (**top**) and wind tunnel (**bottom**) tests.

The MSC/Nastran solver was used for the simulations. The nonlinear behavior of the SMA and its dependence on stress and temperature was handled using the SOL400 solver, which also implements the Auricchio SMA constitutive model through a dedicated card entry, the MATSMA [56].

The models reproducing the whirl tower and wind tunnel demonstrators were made of different elements, with the most solids for the main structure and the SMA and a minority of plates for the sensor supporting beam and the skin. In Figure 6, the two FEM are illustrated. On the top, the naked view of the whirl tower demonstrator is reported, together with the details of the connection flange to the facility. On the bottom, the wind tunnel 4 bays model with the lateral flanges is shown. In Table 9, a summary of the main features of the two models is provided.

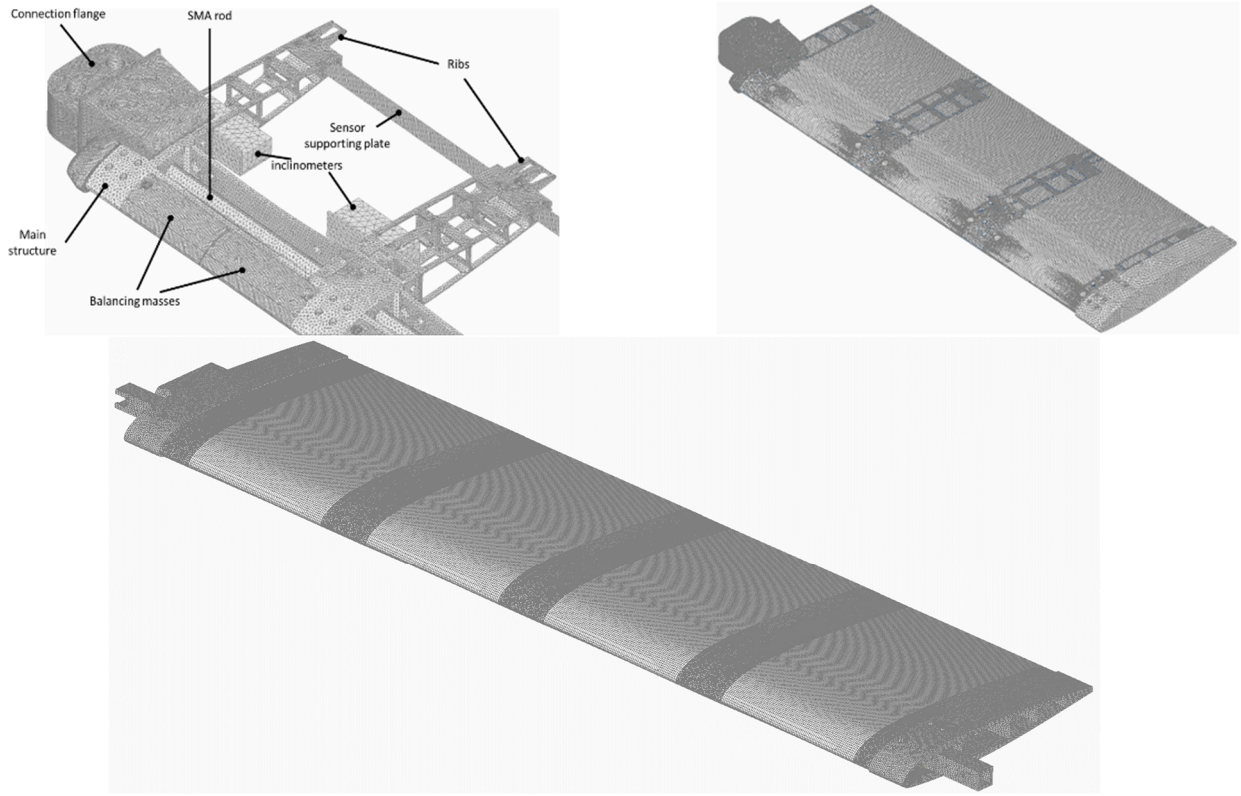


Figure 6. Naked view FEM of the whirl tower demonstrator with detail of the connecting flange (**top**); FEM of the wind tunnel demonstrator (**bottom**).

Table 9. Main features of the wind tunnel and whirl tower structural models.

Parameter	Wind Tunnel Model	Whirl Tower Model
Number of nodes	581,097	409,349
Number of elements	1,782,590	1,443,880
Inertial loads	n.a.	Relevant to an angular speed of 120 rpm
Constraint	Clamped—pinned around the span axis at $\frac{1}{4}$ of the chord	Clamped—free
Aerodynamic loads	Relevant to a maximum speed of 25 m/s Uniform along the span	Relevant to an angular speed of 120 rpm Quadratic along the span

Rigid elements were also used to simulate the built-in connection between the SMA and the main structure. In more detail, they were used to reproduce the embedding of one edge of the SMA at one side of the main structure, the connection of the other edge of the SMA to the crown, and the connection of the crown itself to the other side of the main block. The schematic of Figure 7 provides details of the rigid spider elements used for the pre-load simulation. A yellow spider is used to pre-twist the SMA rod; this twist is transmitted to the crown component using a second rigid element, highlighted in red. Finally, the connection of the crown with the main structure is obtained through a third rigid element, highlighted in red. All the spider elements have the central nodes placed in the middle of the SMA cross-section; in this way, their relative motion can be altered, passing from one simulation step to another and linking through MPC entry the involved dofs.

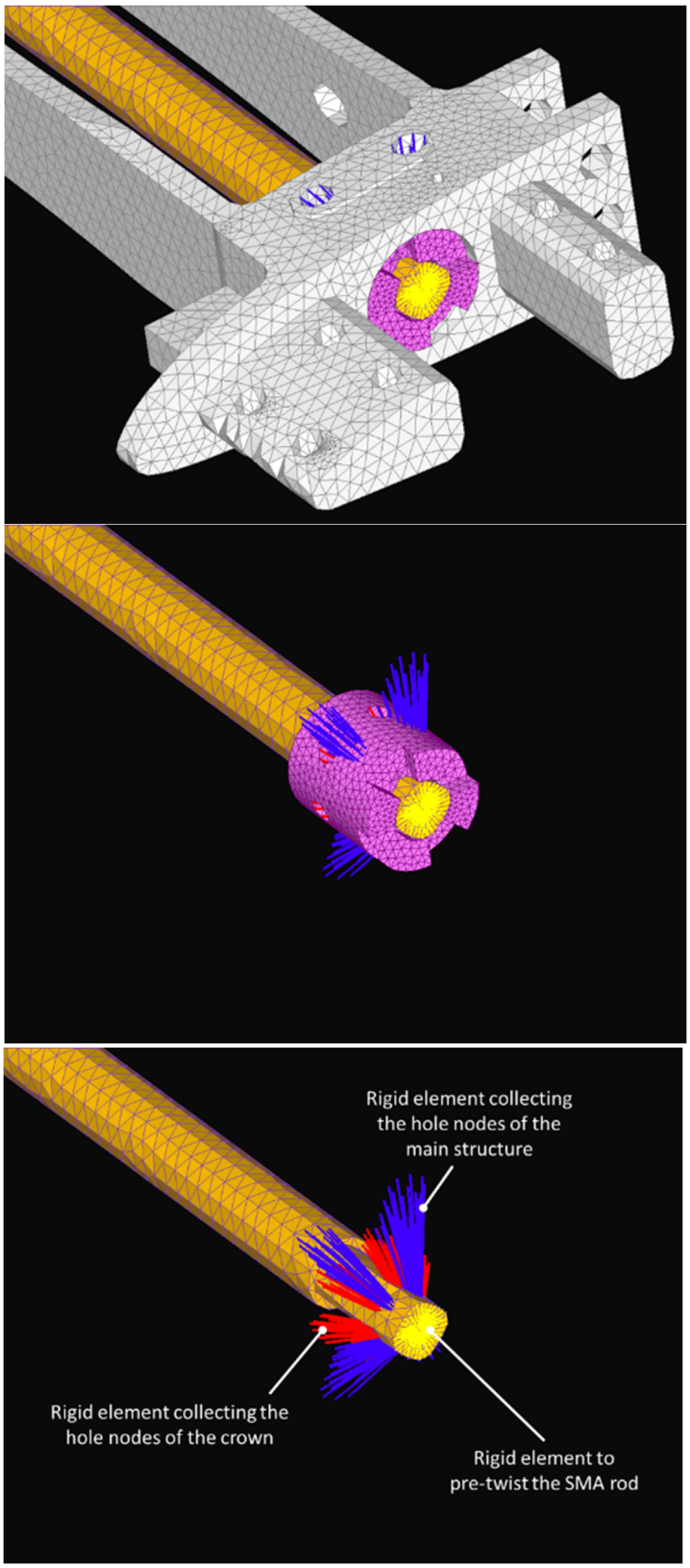


Figure 7. Simulation step of pre-load, connection, and activation operations of the SMA actuators.

The just mentioned model was conceived to simulate the achievable performance and verify the structural integrity of the demonstrators. To this scope, the life phases of the SMA material relevant to the prototype were simulated. In practice, with specific reference to the SMA, the model allows to simulate:

- The pre-twist operation necessary to produce within the SMA rods enough martensite phase to be exploited for the activation (step 1);
- The connection of the twisted edges of the SMA rods to the structure, the subsequent release, and the consequent achievement of the elastic equilibrium (step 2);
- The application of the external loads (step 3);
- The activation of the SMA by heating (step 4).

At first, a twist of 30 deg is applied to the SMA in a clockwise direction through the yellow rigid element (step 1); this also causes the rotation of the crown element connected to the SMA edge through the red rigid element. Then, the central node of this latter element is linked to the corresponding central node of the blue rigid element already connected to the main structure, and the initial twist is removed (step 2); in this way, the SMA tends to recover the angular deformation, but is hindered by the main structure; at the end of this step, the equilibrium is achieved. Then, the external loads are also applied (step 3). Finally, a temperature load is applied to the SMA, enforcing the transformation of the martensite phase produced during the pre-twist and thus transmitting the twist to the surrounding structure (step 4).

Steps 1, 2, and 4 are conceptually common for both the WT and WhT simulations, while step 3 foresees the application of uniform aerodynamic loads along the span for the WT model and of aerodynamics + centrifugal actions on the WhT model. In this latter case, the aerodynamic loads vary linearly and parabolically along the span.

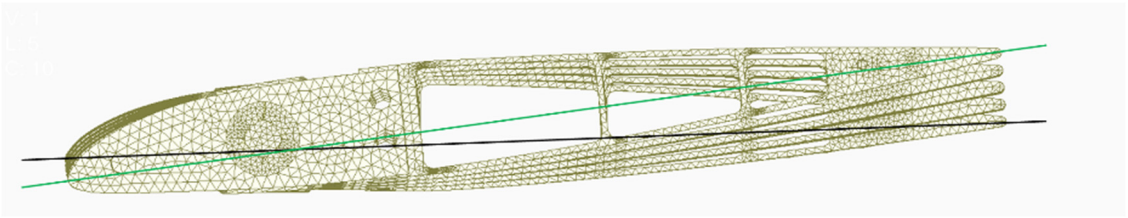
5. Structural Investigations and Twist Performance

This section is devoted to the numerical outcomes for the two configurations previously illustrated. The section has been split into two parts, the former dedicated to the WT and the latter to the WhT model. For both of them, the application of the preload, the external loads (aerodynamics for WT and aerodynamics + centrifugal forces for WhT), and the activation phases are considered.

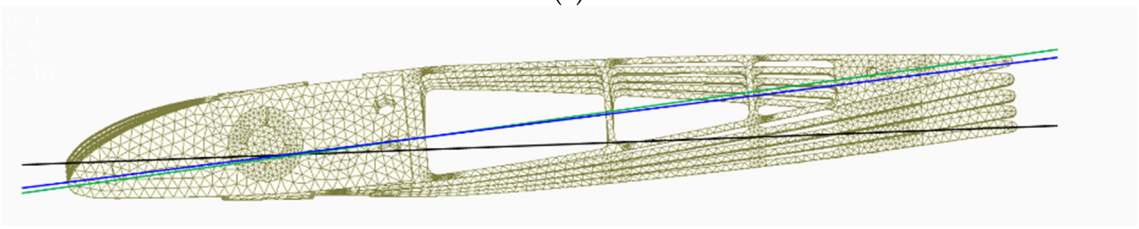
5.1. WT Model

The lateral views of the WT blade model are reported in Figure 8. In the scheme (a), the model in pre-load configuration is depicted. The black line, the track of the chord at the root, represents the reference, while the green line represents the chord of the fourth bay (tip) at the completion of the pre-load operation. In scheme (b), the effect of the aerodynamic actions is illustrated; the fourth blade appears to be upward twisted with respect to the pre-load configuration, as shown by the blue line. Finally, the effect of the full activation of the SMA rods is illustrated in scheme (c); the orange line highlights the pitch ward inclination achieved by the tip blade. It is worth noting that the pivot of rotation (intersection of the different tracks of the chord) does not coincide with the center of the SMA rod. In fact, to meet the tight requirement prescribing that the center of gravity falls within the 1st quarter of the chord, the SMA actuators and, consequently, the spars and the heating coils were placed ahead of the pivot of rotation.

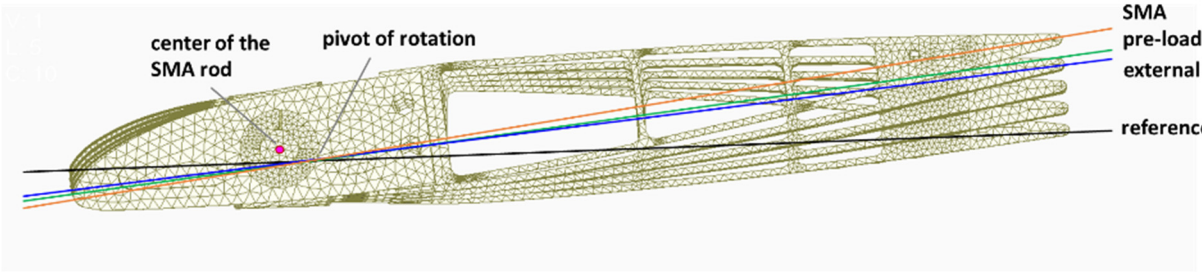
The aerodynamic loads used for sizing the model and predicting its deformed configurations were generated using the XFOIL software [57]. A wind speed of 25 m/s and angles of attack within the range of +/−12 deg were considered, and the most severe load condition was selected for the structural verification. Finally, a temperature of 180 °C was applied to all the SMA rods. The stress levels achieved in the different subparts of the model were reported in the following figures. In the plots of Figure 9, the von Mises stress generated in the three configurations is compared for the main structure. The preload causes maximum stress of 144 MPa on the aluminum alloy structure; this level is slightly reduced to 124 MPa by the upward twist contribution of the aerodynamic loads. Finally, a net increase, up to 159 MPa, was estimated for the SMA switched-on configuration.



(**a**)

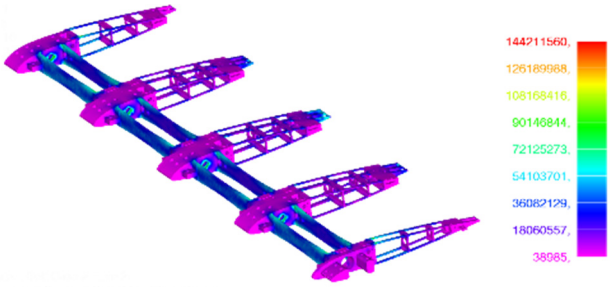


(**b**)

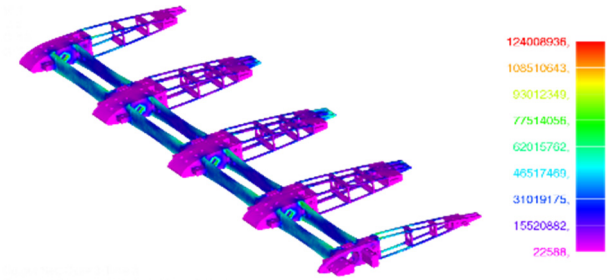


(**c**)

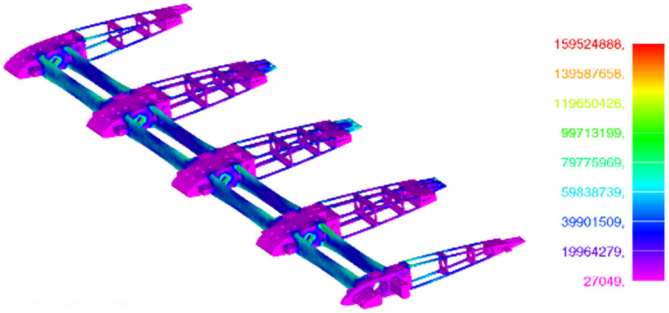
Figure 8. WT model lateral view: preload configuration (blue line, (**a**)), aerodynamic loads (green line, (**b**)), aerodynamic loads + SMA (orange line (**c**)) configurations.



(**a**)



(**b**)



(**c**)

Figure 9. Stress level of the main structure of the WT model: stress level in pre-load (**a**), aerodynamic loads (**b**), and aerodynamic loads + SMA fully on (**c**).

Figure 10 illustrates the stress level achieved on the most solicited ring. Here, the level ranges between 637 and 711 MPa, the latter one achieved for the full activation configuration. Finally, the skin situation is shown in Figure 11; also, in this case, the most critical conditions are achieved when all the SMA rods are fully activated, arriving at a maximum level of 322 MPa against an initial value of 320 MPa in the preload configuration and 305 MPa under the aerodynamic loads. For all the configurations, the diagonal solicitation of the skin caused by the twist (preload or SMA switched on) is evident. In addition, per each configuration, a strain level was observed on the plates with sensors.

Finally, Table 10 provides a summary of the twist angles estimated for all configurations, together with the lowest safety factor achieved among the subparts (main structure, connection rings, skin) and the strain level estimated on the sensor plates. The safety factor of 1.8 was computed for the stress level of 711 MPa of the ring element when aerodynamic loads are applied, and the SMA rods are fully activated. This value was achieved at one edge of the rectangular hole (ring inner view in Figure 10c). Since the refinement of the mesh in the zone is not able to represent a continuous contact transmission between the SMA rod and the ring itself and also considering the local merging of the nodes of the two elements, stress fictitious spikes are expected. A more realistic stress level of 650 MPa averaged in the close zone can be assumed, giving a safety factor of 2. Finally, in Figure 12a, the stress level produced in the SMA rods for the most severe condition, that is to say, in a fully actuated configuration, is illustrated. A maximum von Mises stress of 635 MPa was observed on the lateral neck zones of connection with the main structure (see detail on the left).

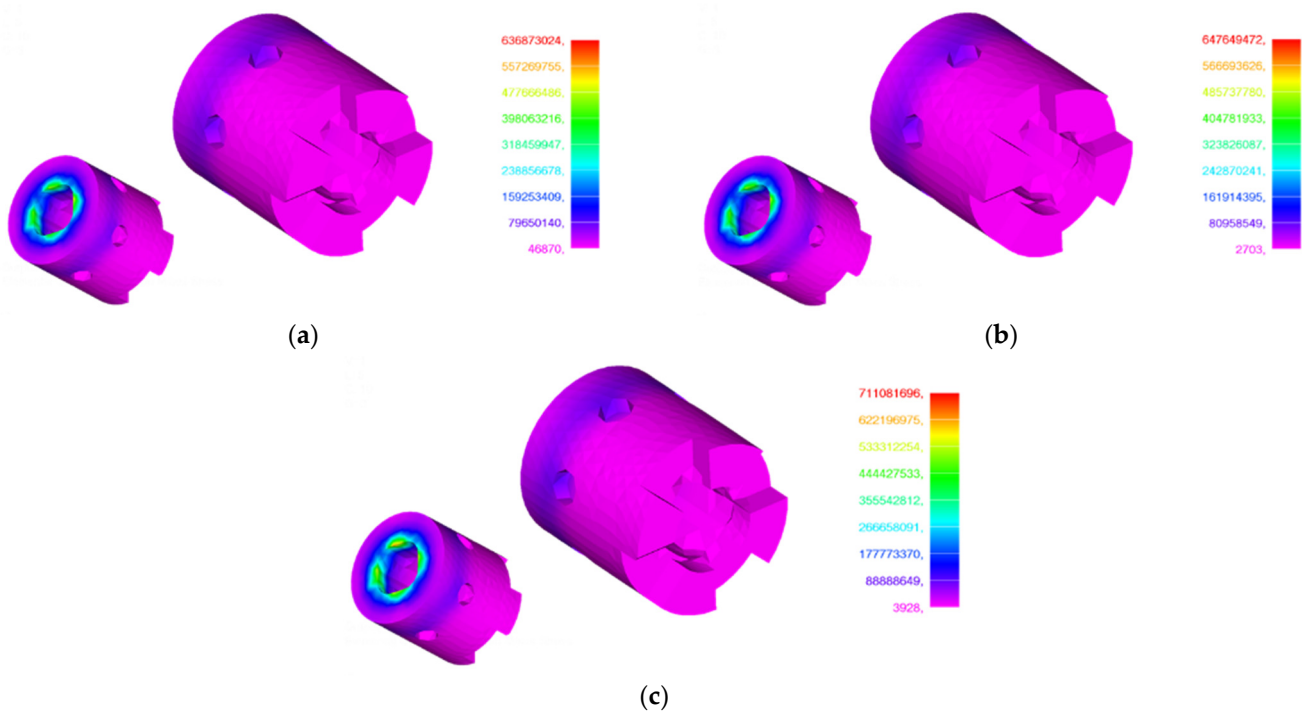


Figure 10. Ring component of the WT model, outer (right) and inner view (left): stress level in the pre-load (**a**), aerodynamic loads (**b**), and aerodynamic loads + SMA fully on (**c**).

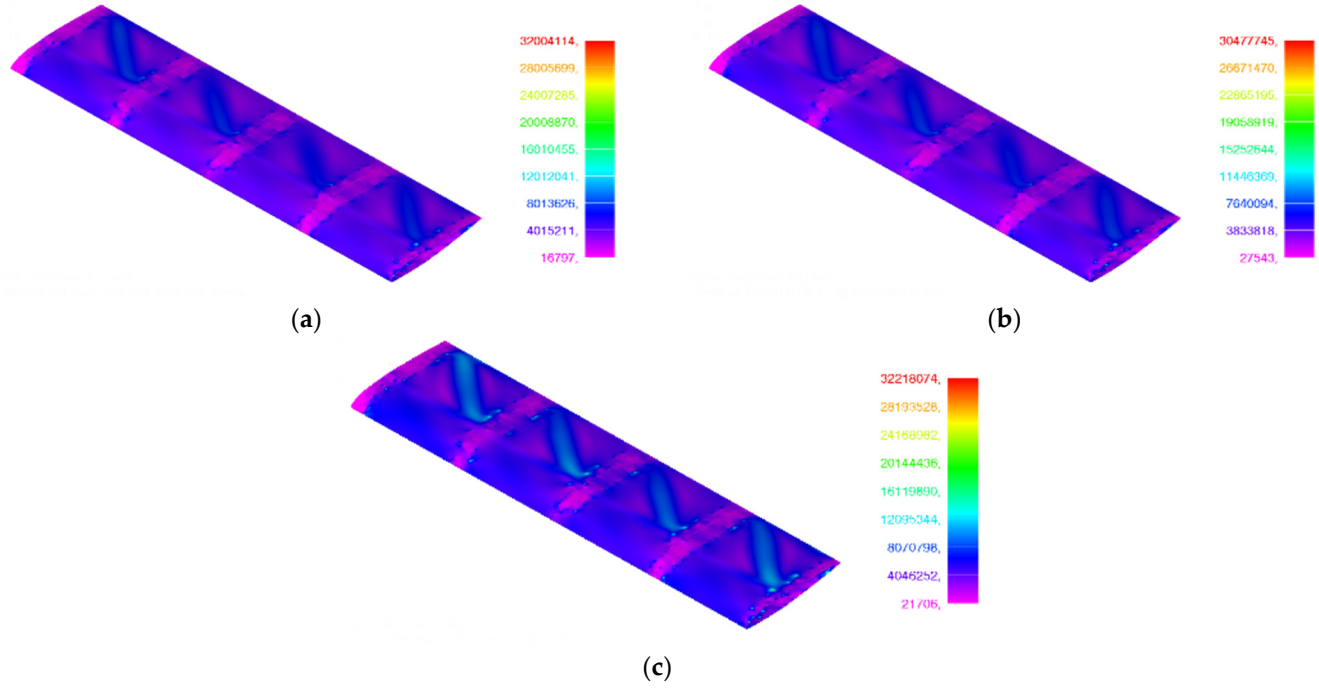


Figure 11. Stress level of the skin of the WT model: stress level in the pre-load (**a**), aerodynamic loads (**b**), and aerodynamic loads + SMA fully on (**c**).

Table 10. WT model twist, minimum safety factor, and strain level on sensor plate vs load condition.

Load Condition (with Reference to Figure 8)	Total Twist Over 4 Bays (Deg)	Delta Twist with Respect to the Pre-Load, Referred to the Entire Blade (Deg)	Minimum Safety Factor	Sensor Plate με	Delta Plate Microstrain
pre-load	4.58		2.1	126.5	
aerodynamic	4.40	−1.01	2.0	115.9	−10.6
aerodynamic+SMA	5.69	6.27	1.8 (*)	159.3	32.8

(*) this value, as explained in the text, was recomputed since it was due to an isolated, unrealistic spike; assuming an average stress in the zone of 650 MPa, a more realistic safety factor of 2.0 was estimated.

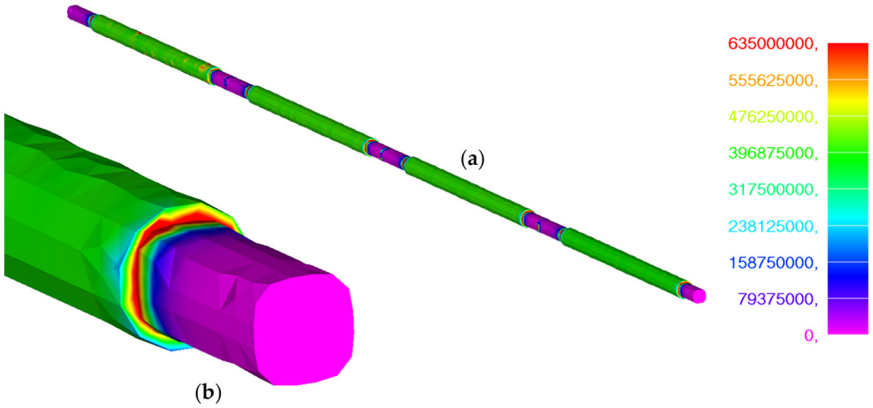


Figure 12. Von Mises stress level within the SMA rods in the WT model for the fully activated condition (**a**) and detail at the neck of the connection (**b**).

5.2. WhT Model

As already done for the WT model and for the 3-bay model realized for the WhT facility, the lateral views for the preload, external loads, and external loads (aerodynamic + centrifugal) + SMA configurations are compared (Figure 13). As done for the WT model,

the XFOIL software was used to compute the aerodynamic loads. The maximum angular speed of 120 rpm prescribed for the tests was used to compute the linear velocity at each span station of the blade segment. The centrifugal loads were also generated using the RFORCE card of the MSC/Nastran solver. Differently from the WT model, it is not possible to identify a unique rotational pivot since the model is not pinned along a span axis, but the tip-free edge can flap under the action of the aerodynamic loads.

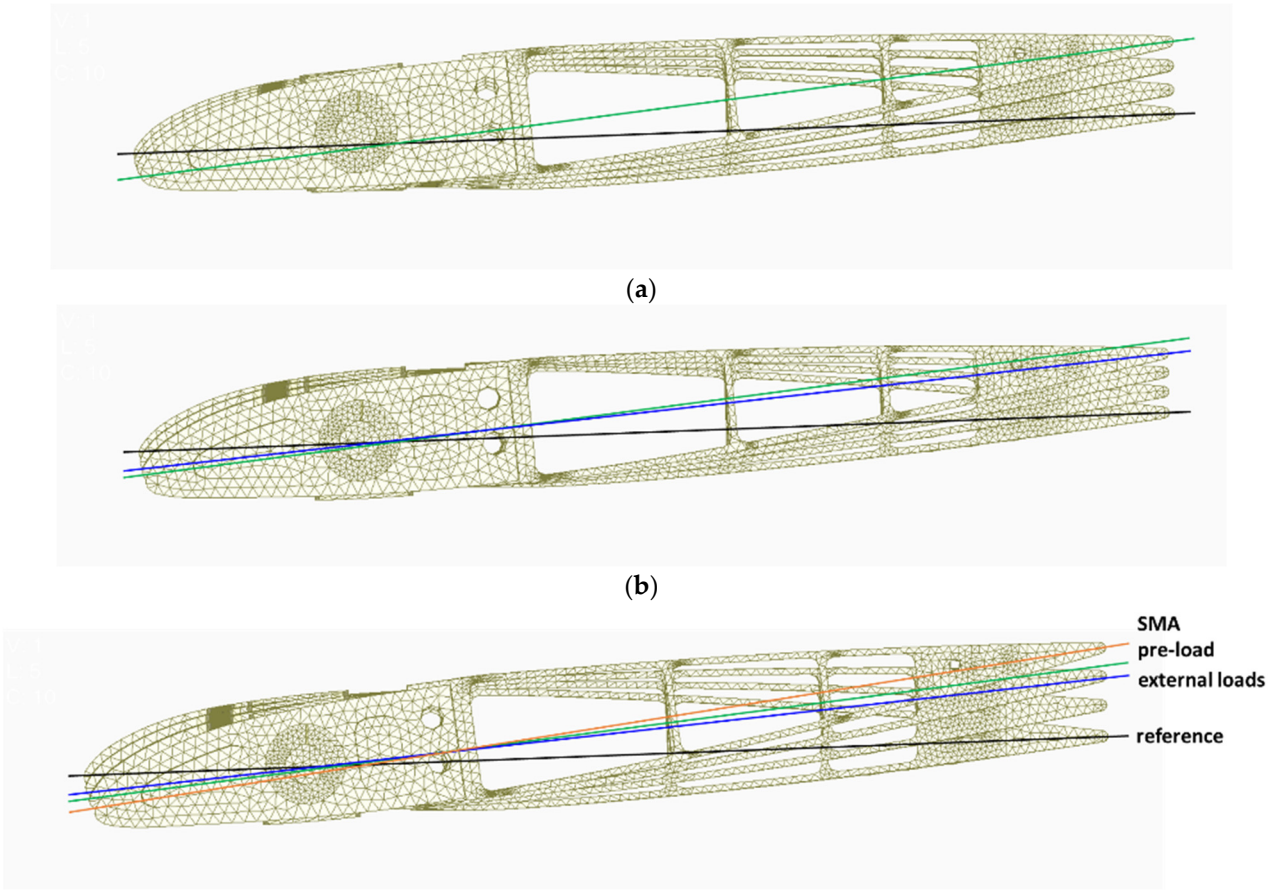


Figure 13. WhT model lateral view: preload configuration (blue line, (**a**)), aerodynamic loads (green line, (**b**)), external loads + SMA (orange line (**c**)) configurations.

In the plots in Figure 14, the stress generated in the main structure is illustrated in the preload condition, in the presence of aerodynamic and external loads, and finally, in the presence of these actions with the SMA rods fully activated. The von Mises stress produced in the configuration of the preload achieves a maximum level of 118 MPa. The application of aerodynamic and centrifugal forces leads to a slight mitigation of the twist with a consequent reduction of the stress level down to 110 MPa. Finally, the full activation of the SMA determines a new maximum of 152 MPa. The stress level produced in the ring transmission element is shown in Figure 15. Also, in this case, the slight increase in stress from the pre-load condition to the application of the aerodynamic and centrifugal forces indicates that the largest contribution to the structural solicitation is due to twist action (preload); the further increase in the stress level occurring for the full activation of the SMA rods again highlights the predominance of the twist actions. The same trend is noticed for the skin element (Figure 16). The rotation of the blade segment at the tip, the minimum safety factor, and the strain estimated on the sensor plate are summarized in Table 11. The resulting safety factors comply with the requirements, with a minimum value of 2.3 in the condition of full actuation. Finally, even in this case, the strain estimated on the sensor plates (8.8 and 70.4 με, in the presence of external forces, with SMAs off and

on, respectively) are compliant with the capability of the acquisition systems. Finally, a situation similar to the WT model was observed for the SMA stress level, with a generally uniform distribution, apart from the neck zone, where a maximum level of 614 MPa was achieved (see Figure 17).

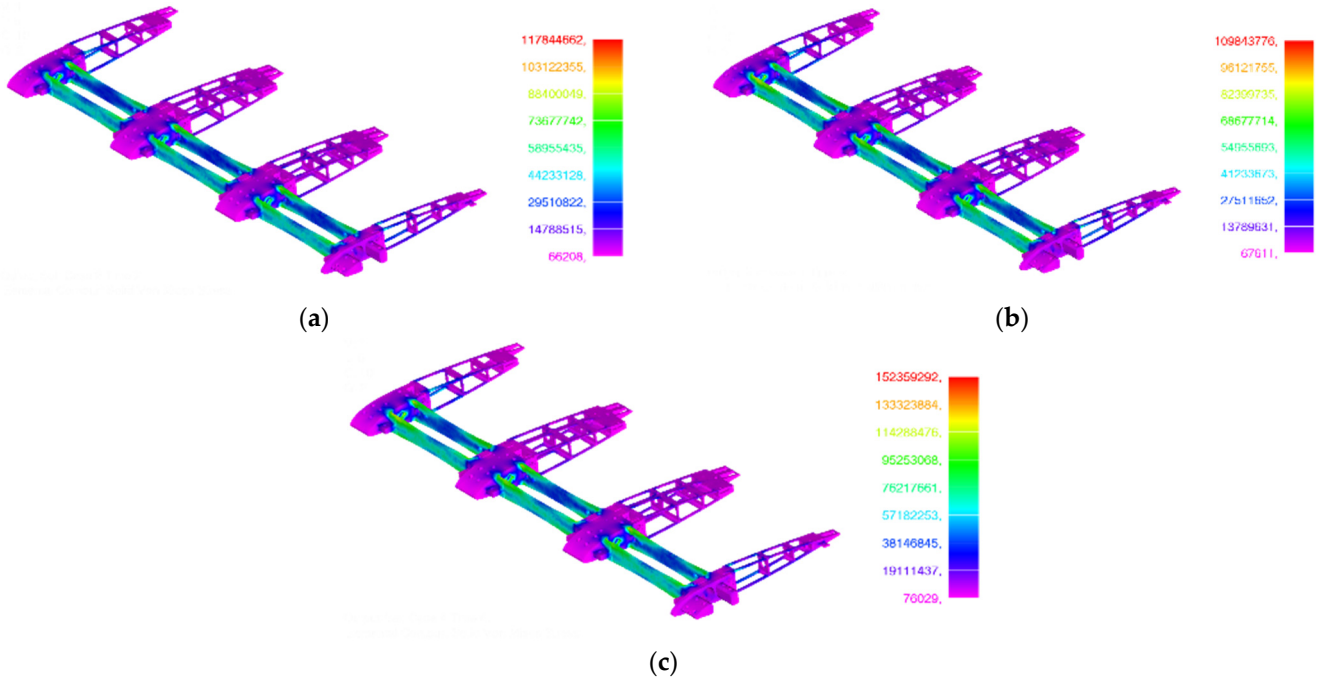


Figure 14. Stress level of the main structure of the WhT model: stress level in the pre-load (**a**), aerodynamic loads (**b**), and aerodynamic loads + SMA fully on (**c**).

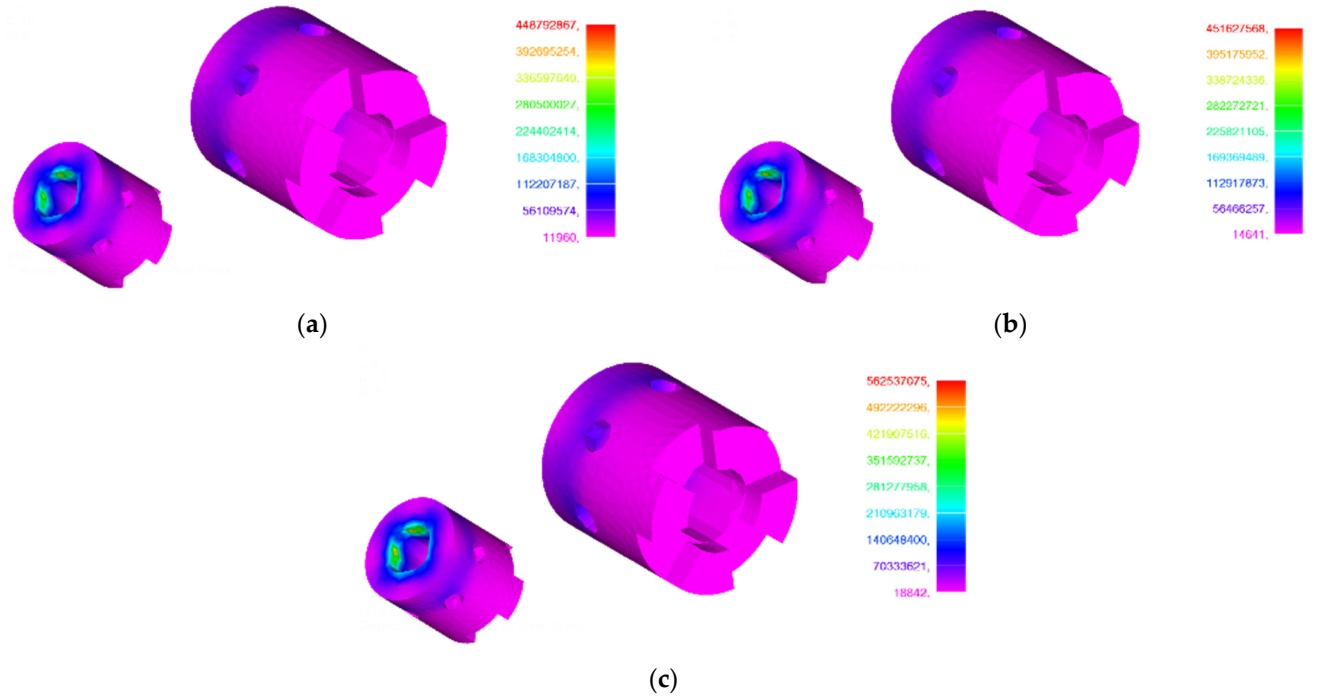


Figure 15. Ring component of the WhT model, outer (right) and inner view (left): stress level in the pre-load (**a**), aerodynamic loads (**b**), and aerodynamic loads + SMA fully on (**c**).

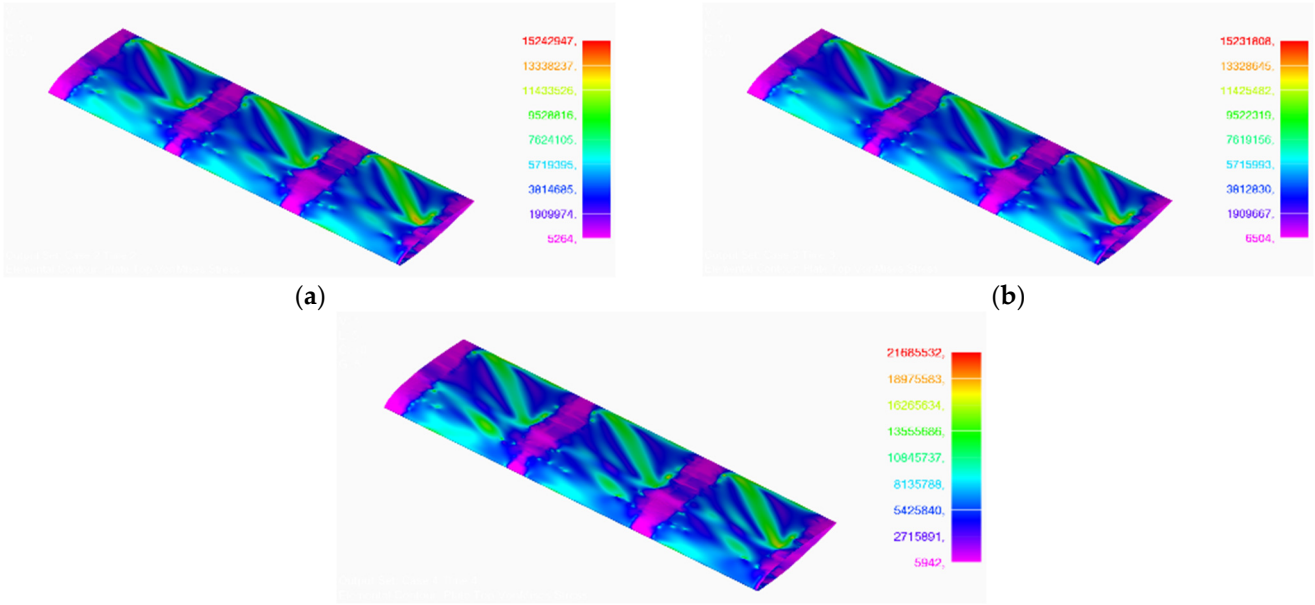


Figure 16. Stress level of the skin of the WhT model: stress level in pre-load (**a**), aerodynamic loads (**b**) and aerodynamic loads + SMA fully on (**c**).

Table 11. WhT model twist, minimum safety factor, and strain level on sensor plate vs load condition.

Load Condition (with Reference to Figure 13)	Total Twist Over 4 Bays (Deg)	Delta Twist with Respect to the Pre-Load, Referred to the Entire Blade (Deg)	Minimum Safety Factor	Sensor Plate Microstrain	Delta Plate Microstrain
pre-load	4.21		2.9	163.0	
aerodynamic + centrifugal loads	4.11	−0.55	2.9	154.2	−8.8
aerodynamic + centrifugal loads + SMA	5.84	9.16	2.3	233.4	70.4

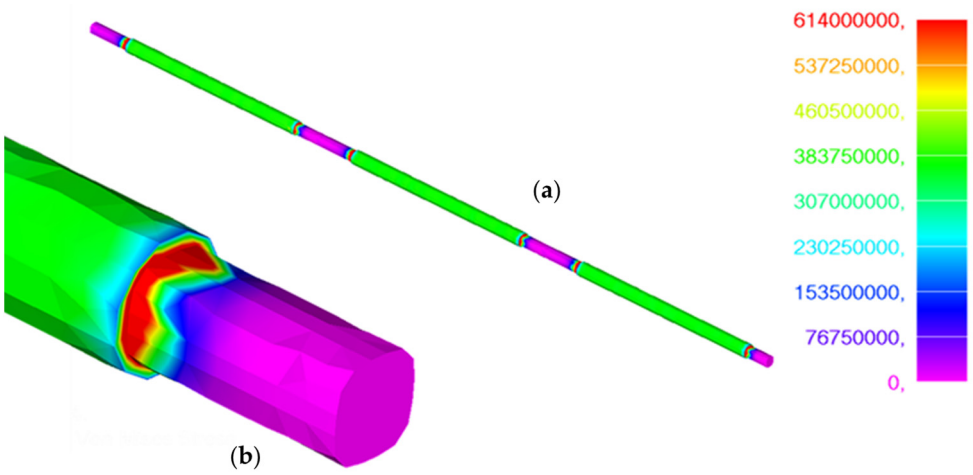


Figure 17. Von Mises stress level within the SMA rods in the WhT model for the fully activated condition (**a**) and detail at the neck of connection (**b**).

6. Compatibility of the SMA Alloy with the Operational Temperatures

In the previous section, the performance of the SMA in terms of transmission of twist was investigated. In this section, attention is instead paid to the compatibility of the alloy with the requirements relevant to the temperature.

According to the requirements, the SMA alloy must start working at a temperature over 90 °C to avoid any undesired activation due, for instance, to warm environmental conditions; at the same time, it has to finalize the twist transmission within 180 °C to prevent any overheating safety issue.

To verify the compliance of the alloy with the minimum activation temperature of 90 °C, the percentage of transmitted twist to a single cell was plotted against the imposed temperature (Figure 18). The activation of the alloy starts at a temperature of 95 °C, as the curve starts arising, while it achieves a plateau at 180 °C.

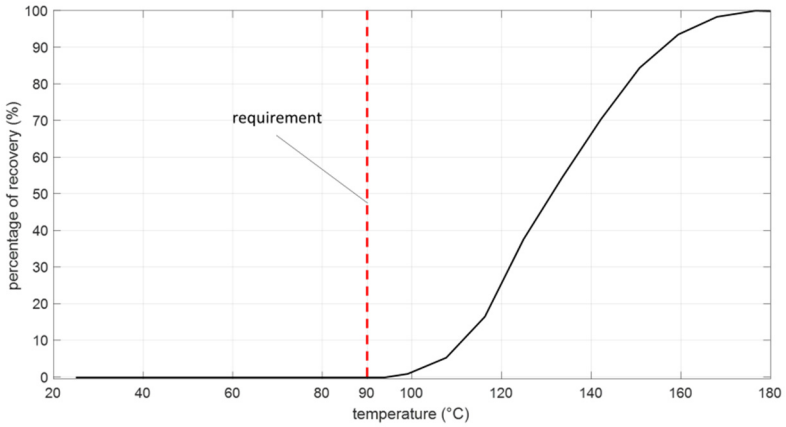


Figure 18. Percentage of twist transmitted vs. temperature.

Thermal analysis investigations were addressed to verify the compliance with the requirement of full activation at 180 °C. Dedicated finite element models were realized for the WT and the WhT prototypes to support thermal analyses and take into account the different heat transfer conditions characterizing the two environments.

Figure 19 depicts the model used for the WhT demonstrator, constituted by 141.376 solid elements. The structure of the ribs was replaced by solid elements, whose larger thermal capacity tends to absorb greater heat quantity than the real structure, made of truss-like elements. In addition, the model is naked to further increase the heat transfer with the environment and, thus, the thermal losses.

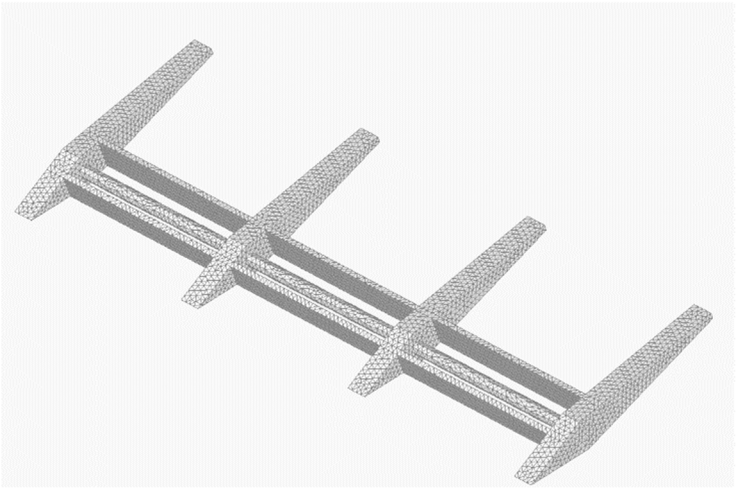


Figure 19. The finite element model used for the thermal analysis of the WhT blade segment.

A steady state thermal analysis was implemented to estimate the power necessary to keep a uniform temperature on the SMA rods at regime condition, that is to say, after having reached the desired temperature of 180 °C. The conduction among the solid parts was considered, assuming the thermal conductivity and heat coefficients reported in Tables 2 and 3. Convection and radiation modes were also implemented, assuming an environmental temperature of 25 °C. The convection coefficient, h, was computed as a function of the speed v, through the following formula [58]

$$h = 12.12 - 1.16\,v + 11.6\,v^{0.5} \quad (1)$$

valid in forced convection conditions.

6.1. WT Model

Since the model is supposed to be pinned on the two edges and, thus, in contact with the structure of the wind tunnel, the interfaces of the lateral ribs were supposed to be at a temperature of 25 °C. Using the above-mentioned Relation (1) and considering the maximum velocity of 25 m/s foreseen for the tests, a convection coefficient of 41.1 W/m^{2}K was computed. Under these conditions, a uniform power adduction of about 65 W per SMA rod was necessary to achieve the temperature distribution illustrated in Figure 20. More than 50% of the span of the rods is at a temperature of 180 °C, decreasing to about 60 °C at the edges. Although this estimate is conservative regarding power losses, it points out the necessity of methods to make the temperature along the rods more uniform. In this sense, heating coils with more turns at the edges are required to increase the power adduction where the losses are more relevant. Finally, to have an idea of the impact of the power on the rapidity of activation, the other two values, 130 and 325 W (2 and 5 times the power of 65 W), were investigated. The plot in Figure 21 illustrates the time histories of the temperature against the power supply. The achievement of the target temperature of 180 °C occurs at different times, following the exponential trend illustrated in Figure 22.

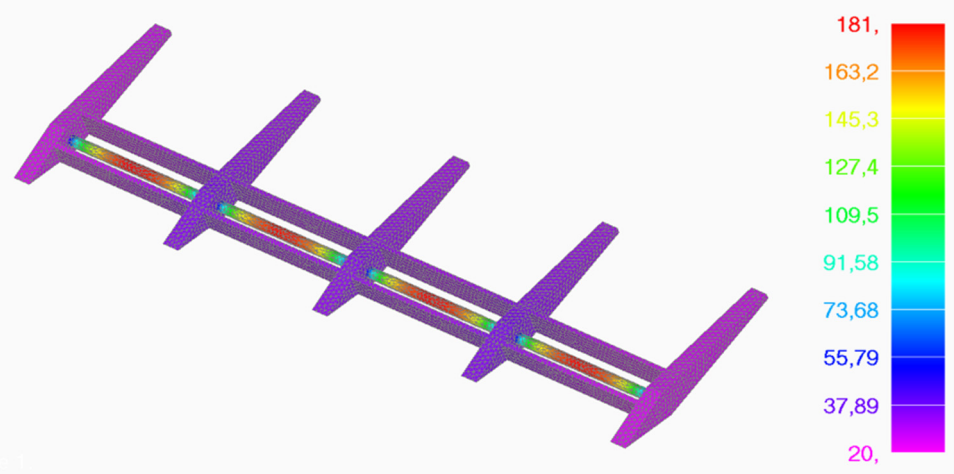


Figure 20. Steady-state thermal analysis on the WT model, assuming a power adduction of 65 W per SMA rod at regime.

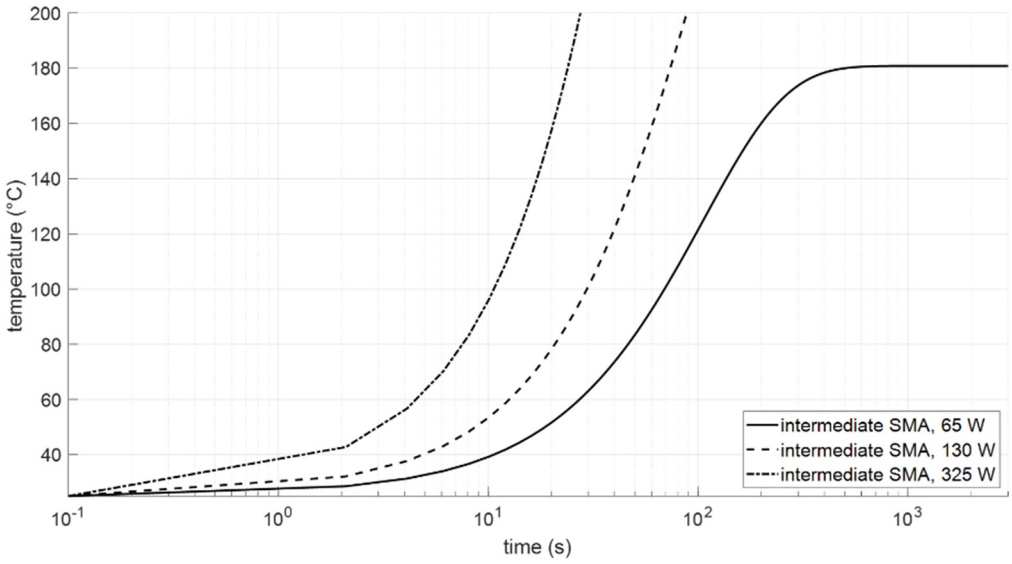


Figure 21. Heat transfer analysis: temperature in the middle of the SMA rods of the WT model vs. power vs. time.

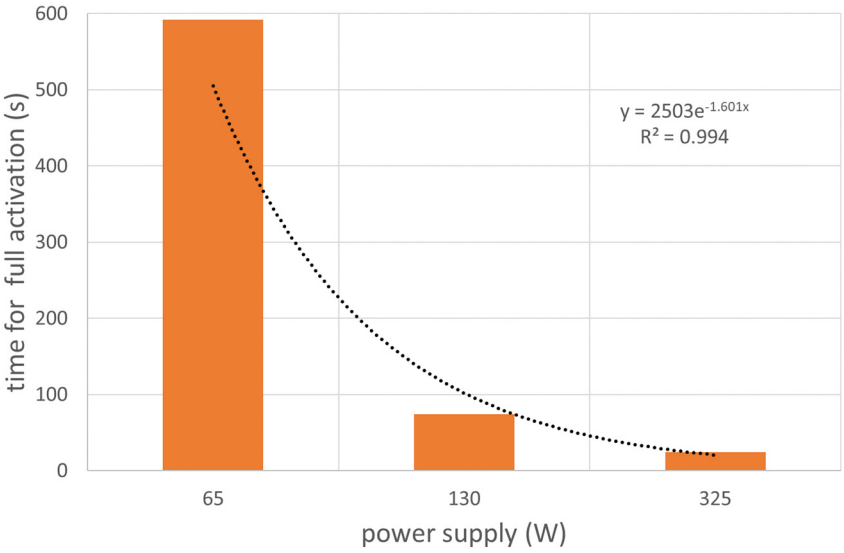


Figure 22. Time required for the full activation of the SMA rods of the WT model vs power supply.

6.2. WhT Model

A temperature of 25 °C (room temperature) was imposed on the root rib of the WhT model, being clamped to the test facility. Three different values of the convection coefficient were computed for each of the three bays using Formula (1), considering that the speed varies linearly against the span, from a minimum of 5.5 m/s (inner cell) to a maximum of 12.1 m/s (outer cell) corresponding to a rotating speed of 120 rpm. As already done for the WT model, a heat flux was applied to the surface of the SMA rods to simulate the effect of the heating coils. Figure 23 illustrates the temperature distribution obtained for a power adduction of 30.5 W per SMA. A warmer zone is evident for each rod, interestingly more than 50% of its length. However, the non-uniform value of the speed towards the span is evident, as the outer rods' temperature is lower for the more effective convection.

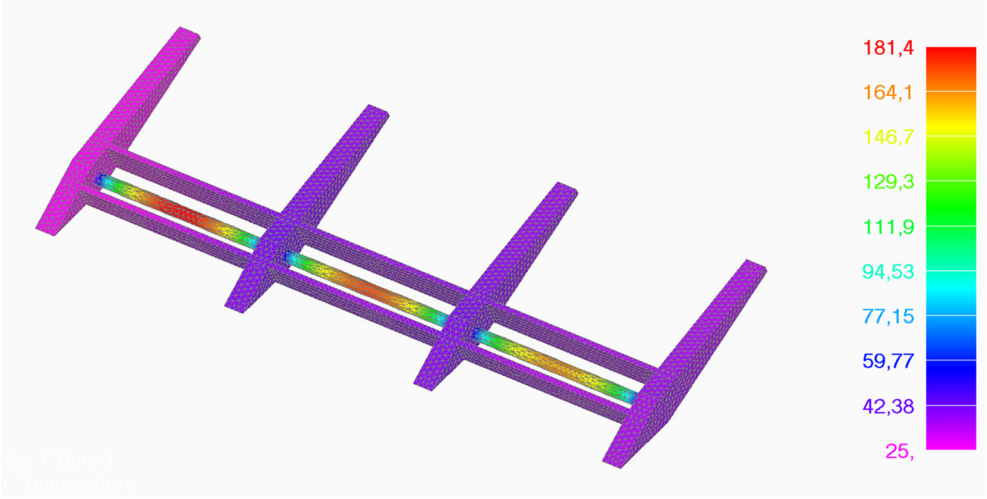


Figure 23. Steady-state thermal analysis on the WhT model, assuming a power adduction of 30.5 W per SMA rod at regime.

To have an idea of the time required for the activation, that is to say, for achieving the maximum temperature prescribed (180 °C), a heat transient analysis was also implemented for this model. The plot in Figure 24 compares the time history of the temperature in the middle of the three rods versus the power supply. The power supply of 30.5 W (solid line) assures a steady condition after about 418 s. A double power of 61 W dramatically reduces the time to achieve the target of 180 °C down to about 116 s. Finally, a power supply 5 times the one considered for the steady-state analysis, 152.5 W, further reduces this time to 40 s.

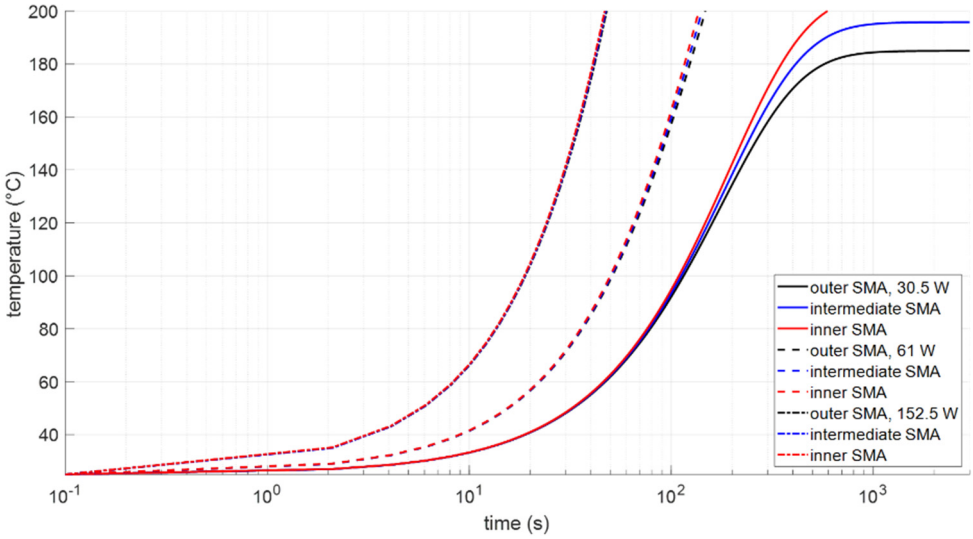


Figure 24. Heat transfer analysis: temperature in the middle of the SMA rods of the WhT model vs. power vs. time.

As already done for the WT model, in this case, a bar chart was built to highlight the trend of the time necessary for the full activation against the power supplied (Figure 25).

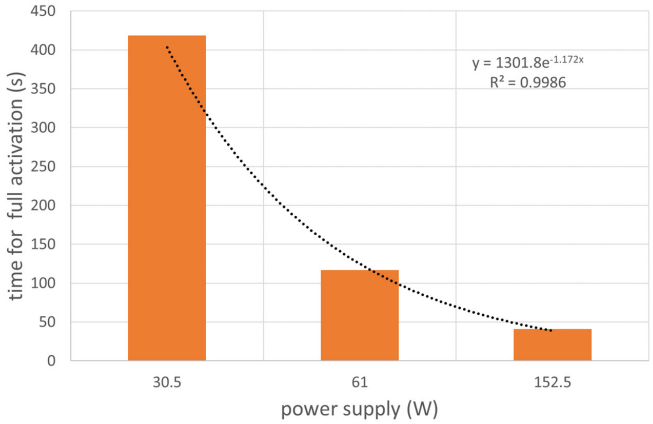


Figure 25. Time required for the full activation of the SMA rods of the WhT model vs. power supply.

7. Mass Distribution

In this section, attention is paid to the requirement of mass distribution (see Table 1). The allowable position to avoid instability must fall within the 1st quarter of the chord of the airfoil. In this condition, the point of application of the aerodynamic actions is located downstream of the center of gravity, and any perturbation leading to an increase in the angle of attack is compensated by stabilizing forces.

To verify compliance with this requirement, the computation of the position of the center of gravity was addressed using the DMU.

The position of the center of gravity does not depend on the type of demonstrator since both of them are constituted by the same basic cell; it resulted at 48 mm from the leading edge, corresponding to 18.3% of the chord, well within the requirement (25% of the chord). Its position is highlighted in the top view of a naked cell, illustrated in Figure 26.

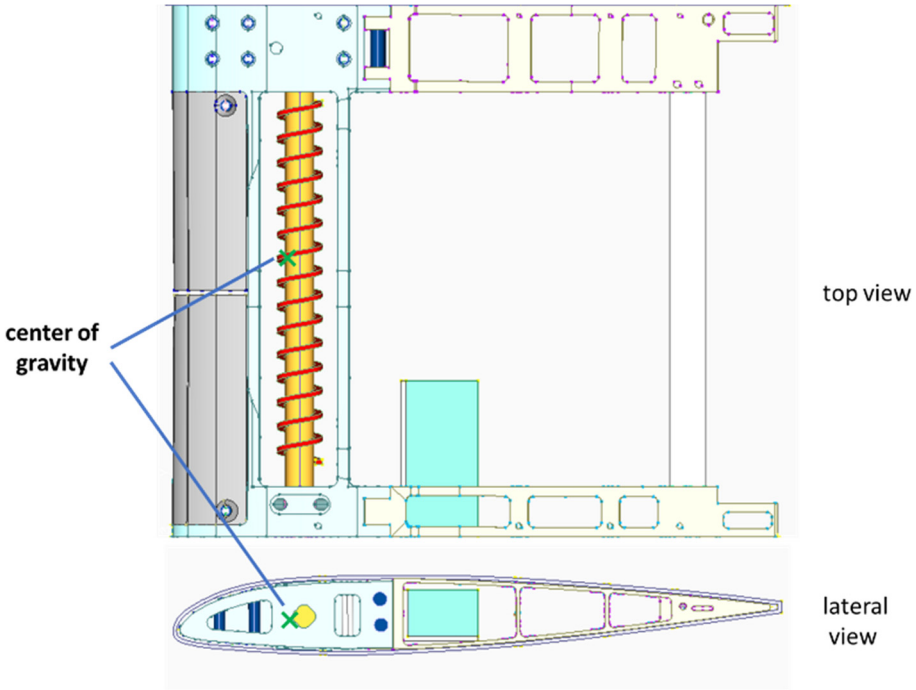


Figure 26. Location of the center of gravity (top and lateral view of the cell).

8. Performance vs. Requirements

A critical overview of the results presented above was organized against the requirements. A summary of this comparison is reported in Table 12.

Table 12. WT and WhT models requirements against performance.

Parameter	Requirement	Z	Performance of the WT Model	Performance of the WhT Model	Notes	Score Formula
Additional twist (deg/R)	≥8 deg/R, pitchward		6.27 deg/R	9.16 deg/R	The obtained performance is lower than the one required for the rotorcraft; however, it refers to a clamped-pinned configuration that penalizes the transmitted twist.	$\frac{\vartheta}{\vartheta_{req}}$
Safety factor	≥2		2.0	2.3	For the WT model, as already discussed, a lower safety factor (1.8) was observed for the ring connection. However, considering that the critical stress was achieved only for a local spike, an average value was computed on the zone around, with a result compliant with the requirements.	$\frac{\vartheta}{\frac{\sigma_{allow}}{\sigma}}$
Activation temperature of the SMA	≥90 °C		95 °C	95 °C	The requirement is satisfied. Even though room temperature is expected within the test facilities, the current value supports the potential use of the system for a typical aeronautic operational scenario [−50, +80] °C	$\frac{T_{start}}{T_{start,\ \ req}}$
Maximum temperature of the heating source	≤180 °C		Achieved	Achieved	A dedicated control logic was defined, and in case of fault, the fuse on the temperature and current were integrated within the power supply circuit.	$\frac{T_{finish}}{T_{finish,\ \ req}}$
Allowable SMA stress	≤700 MPa		635 MPa	614 MPa	Satisfied	$\frac{\sigma_{SMA,\ allow}}{\sigma_{SMA}}$
Mass distribution	Center of gravity placed within the 1st quarter of the chord (25% of *c*)		18.3% of c	18.3% of c	Satisfied with an adequate stability margin.	$\vartheta_{incl,\ req}$
Inclinometer measurement range and accuracy	range no smaller than [−45, +45] deg accuracy ≤ 0.1 deg		−45,+45 deg Accuracy: 0.1 deg	−45,+45 deg Accuracy = 0.1 deg	These requirements were satisfied by the selected sensor.	$\frac{\vartheta_{incl,\ req}}{\vartheta_{incl}}$ $\frac{acc_{incl}}{acc_{incl,req}}$
Strain measurement range and accuracy	Range no smaller than [−2000, +2000] με Minimum strain (absolute value) ≥ 5 με		Maximum deformation: 159.3 με Minimum strain (absolute value): 10.6 με	Maximum deformation: 233.4 με Minimum strain (absolute value): 8.8 με	The maximum strain for both demonstrators occurs in the full activation condition, and results are well within the range. The minimum strain estimated is well within the strain difference between the condition of preload with external loads and the condition of fully activated (32.8 and 70.4 με for WT and WhT); this assures adequate discrimination between the intermediate configurations.	$\frac{\varepsilon_{req}}{\varepsilon}$ $\frac{\Delta\varepsilon}{\Delta\varepsilon_{req}}$
Cabling and routing	All the cabling must exit from one edge of the demonstrator.		Satisfied	Satisfied	All the ribs present openings to allow the passing of sensing and supply cabling. The area of the openings is enough to allow the passing of the entire bundle through the rib at the root.	1

Starting from the additional twist obtained through the SMA actuators, different performance was obtained for the WT and WhT prototypes: 6.27 against 9.16 deg/R. As discussed, this can be attributed to the different constraint conditions. In the case of the WT model, the clamped-pinned condition limits the transmission of twist, hindering the spanwise displacement. However, this constraint configuration imposed by the facility does not describe the real working of the architecture that is supposed to work in clamped-free conditions, for which the requirement is over-satisfied by about 14%.

The stress level aligns with the requirements, having achieved a minimum value of 2 and 2.3 for the WT and the WhT models, respectively. The different stress performance between the two prototypes is again due to the constraint conditions that, in the case of the WT model, led to a more pronounced stress concentration. In terms of stress, the SMA material appears compliant with the requirement that, as specified above, in this case, it is not expressed in terms of the safety factor but in terms of stress. Also, in this case, the trend of the stress level between the two models is confirmed with a slightly higher value for the WT prototype (635 against 614 MPa). It is worth noting that both values are slightly lower than the allowed stress of 700 MPa. This small margin meets the need for a high-stress level within the SMA elements to produce enough martensite phase exploitable for the twist recovery. However, possible SMA failure events due to the high stress level are mitigated by the specific layout that incorporates the elements and, thus, limits the potential projection of debris.

The temperature requirements were met; that is, starting the activation over 90 °C and completion at a maximum temperature of 180 °C, in terms of intrinsic transformation properties of the SMA and in terms of heat transfer. Furthermore, when the thermal analyses of the impact of the power supply on the temperature profile were investigated, we found the minimum power needed for the asymptotic achievement of 180 °C. A higher power supply can be provided, but, in this case, the use of a logic of control must be considered.

The layout considered is compliant with the requirement on the position of the center of gravity with a margin of about 14%, which can be useful in case of the possible installation of sensors not foreseen by the original design. Moreover, if needed, further external masses can be added at the leading edge, at least for the WhT tests, whose focus is mainly on the functionality under centrifugal actions and not on the aerodynamic performance. However, additional external masses must be adequately evaluated for their impact on the stress distribution and level.

The deformation level estimated on the plates integrated with fiberoptics also resulted in line with the requirements in terms of maximum range and minimum value to be acquired. The maximum strain estimated was 233 $\mu\varepsilon$, almost one order lower than the prescribed range; this seems a good compromise between the measurement capability, the structural limit of the sensors, and their bonding. Moreover, the minimum variation of strain, 8.8 $\mu\varepsilon$, passing from one configuration to another, results in an acceptably higher than the minimum strain detectable by the sensors, 5 $\mu\varepsilon$, allowing the detection of intermediate configurations. Finally, in line with the requirements, the inclinometers selected for the application offer the possibility of supporting the dedicated logic of shape reconstruction based on strain measurements.

Then, the internal layout, despite the small room, was conceived to host the cabling necessary for the sensors and the heating coils. Two considerations should be made in this regard. First, the truss-like structure that characterizes all the ribs is prone to the passing of the cables towards the span direction, up to the rib at the edge; second, holes were foreseen in the rear spars of each cell to allow the crossing of the heating coil cables towards the rear region of the cell and, then, bundle them with the other cables of the sensors.

Finally, a radar plot was prepared to quickly compare the performance obtained for the two demonstrators (Figure 27). The formulas reported in the last column of Table 12 were used to weight the achieved performance against the requirements. Scoring lower or higher than 1 indicates under or over-satisfaction of the requirement. When a unitary value

is specified, the requirement is satisfied by the identification of a specific component as a sensor. Apart from small deviations in the transmitted twist, the stress level in the structure, and the strain increment from one configuration to another, the two demonstrators are equivalent.

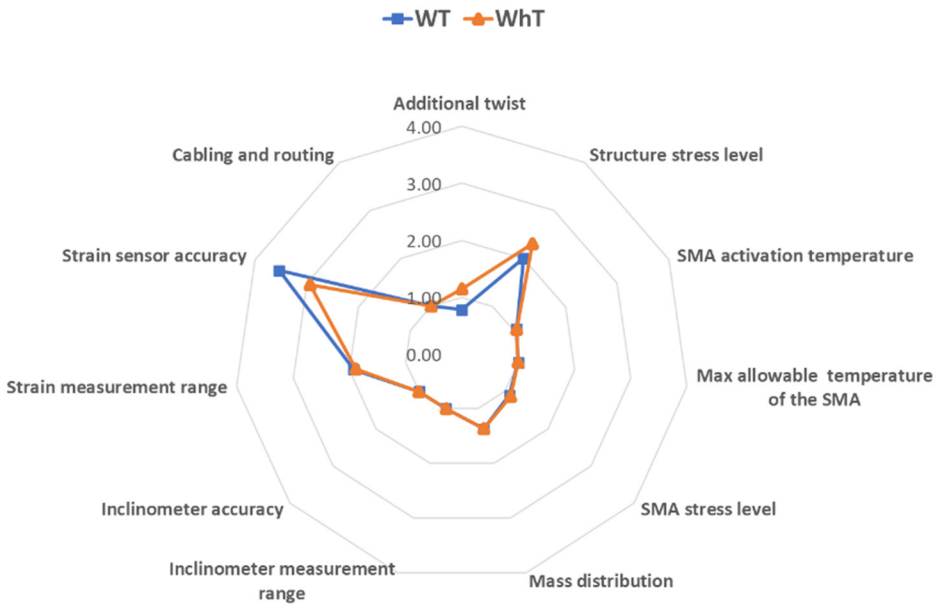


Figure 27. WT and WhT model performance comparison.

9. Critical Analysis of the Layout Adopted for the Demonstrators

Even if the same cell architecture was adopted to build the two demonstrators, the operational scenario they were conceived for and the different constraint conditions determine different performances, as discussed in the previous section. That said, it is important to highlight the advantages and drawbacks presented by the architecture for these different test environments.

A first consideration concerns the way the prototypes absorb the twist generated by the SMAs. The higher twist obtained for the WhT model, not constrained at the tip, gives a perception of the role of the relative movement among the rib planes. A coupling among twist and flap and lagging dofs can be assumed. In fact, the layout, characterized by two spars connecting the ribs on the forward part, favors the relative movement of the aft parts of the airfoil, in practice enabling load absorption and redistribution along the span direction.

The just mentioned aspect, representing an advantage for the WhT configuration and, thus, for the real working modality of the blade, has to be accurately considered for its impact on the strain measures. The sensing system proposed in this work is based on a plate element clamped at one rib and sliding within a rectangular-shaped hole in the opposite rib. This specific constraint condition allows the transmission to the plate of the relative motion of the ribs; however, the distance of the plate from the torsional actuator, from one side, enhances the strain measured and, from the other side, stiffens the structure and, thus, hinders the twist actuation. To mitigate this last drawback, a weaker constraint was considered for one edge of the plate, allowing its sliding. However, when the relative movement of the ribs along the span is allowed, jamming and/or gaps can occur in the sliding guide, altering the measure. This problem is further emphasized when centrifugal forces are present. In this sense, the proposed sensor layout is more suited for the WT model.

Another important aspect that differentiates the two demonstrators is represented by the interface with the supply and the measurement equipment. The unavoidable presence of sliding connections for the WhT model leads to issues that must be accurately considered, even in view of a real application. As already discussed, noise can be generated by the

floating nature of the connection. This has an immediate impact on the quality of the measure and may require off-line filtering operations. However, the most relevant impact is in terms of safety. The system is equipped with a logic of feedback on the temperature, and any error on the signal may alter or make, in the worst case, ineffective control. The most severe consequence is the trespassing of the allowable thermal limits of the skin material. Current and temperature fuses must be inserted in the supply circuit to prevent this issue.

Given temperature problems, the different behavior of the two models is worth noting. Due to the narrow available room, no refrigerating systems were considered; cooling down is obtainable only through the control logic and the intrinsic capacity of the system to disperse heat. As shown by the thermal analyses, the higher speed makes the WT model once again safer.

10. Conclusions and Further Steps

In this paper, the modeling of a morphing architecture aimed at altering the original twist of a blade of the main rotor is presented. The architecture was conceived to be modular, that is to say, constituted by different structural elements, called cells, connected to each other towards the span direction to form a blade segment. This approach was implemented to define two models destined for wind tunnel and whirl tower tests, respectively.

At first, the definition of the requirements was addressed. In this phase, an attempt was made to conciliate the restrictions of the test facilities with some requirements typical of a real application. This work led to an architecture not applicable for flight but with room for improvement. To cite an example, the current stiffness, even if similar in order of magnitude to that of the real blade, is about 20% of it. This choice allowed the required twist with a stress level compliant with the restrictions of the facilities. Higher rigidities and, thus, more robust structures would have required a higher authority of the SMA elements, still obtainable by increasing their radius. However, the pre-load would have needed the application of greater forces, making the integration process more challenging from a safety point of view.

After having faced the requirement task, the layout was defined. Some aspects were particularly considered. First is the structure's capability to absorb the typical loads acting on a blade, keeping a stable configuration from the inertia point of view. Second, its specific compliance to the twist actuation within the safety prescription. Third, the possibility of measuring the current shape through a dedicated sensor network. All these primary aspects concurred with the identification of the architecture described in the first part of the work. The layout is constituted by the main solid metallic structure absorbing loads through a couple of shaped spars. Their location, the placement of the SMA element and of the heating coil between them, and the presence of additional interior masses on the leading-edge region contributed to moving forward the center of gravity. Truss-like ribs, robust but at the same time, do not significantly alter the mass distribution and assure an adequate transmission of the twist along the chord. Plate elements were then integrated between the ribs of each cell, very close to the trailing edge, where the displacements due to the twist were amplified. The strain measurements at specific stations of these plates, suitably elaborated by a dedicated logic of shape reconstruction, can give precious information regarding the type of morphing (flap bending and/or twist) and magnitude.

After having assessed the layout, its behavior was investigated. At first, the focus was on the structural performance and the twist transmitted by the SMA elements, assuming the constraint conditions and the most severe load sets foreseen in the test campaigns. The specific nature of the SMA required the adoption of dedicated tools capable of simulating the constitutive law of the alloy, jointly involving both the temperature and the stress level. Nonlinear static analyses were implemented, describing, at first, the pretwist of the SMA and the integration within the structure and, then, the activation of the alloy through heating. The results were expressed in terms of stress level within the structure, strain estimated at the sensor plates, and transmitted twist. After having critically examined the results and having tracked a comparison between the WT and WhT configurations,

the estimate of the power supplied to heat the SMAs was addressed. Attention was paid to the minimum power needed to fully and uniformly activate the SMAs, respecting the restriction of the facilities. A logic of control was judged necessary jointly to fuse within the power supply circuit to avoid any overheating. Another critical aspect was represented by the level of activation against the temperature profile. In this regard, even if room temperature is foreseen for the tests, the requirement of an activation over 90 °C was considered and met in view of an application within a real operational scenario.

The encouraging results achieved in this application led to the realization of the prototypes for the WT and WhT experimental campaigns. After the completion of the functionality and commissioning tests, the devices were delivered and tests executed in the facilities, generally confirming the modeling predictions and the effectiveness of the concept that was considered worth intellectual protection.

One of the most important aspects of the modeling approach herein developed is represented by the simulation of the different phases that characterize the realization and the functioning of the SMA twist device. At first, the preload phase was modeled. The peculiar nature of the SMA, requiring enough martensite for the strain recovery, led to considering a specific integration approach, consisting of pre-twisting and then connecting the SMA to the structure to achieve the elastic equilibrium. This process is strictly non-linear for the SMA constitutive law and the impact of the stress level on the global stiffness matrix. A nonlinear solver was necessary to simulate the process. Moreover, passing from the pretwist operation to the connection with the structure, specific dofs were connected. In this way, the process was faithfully replicated. After the integration phase, the effect of the applied loads was simulated. The sequence of the operations occurring during the test campaigns was respected in the simulation. Thus, first, the external loads (aerodynamics for the WT and aerodynamics + centrifugal forces for WhT) were applied, and their effect was predicted within a dedicated simulation step. Then, the SMAs were actuated, and their effect on the deformed shape and in the presence of the external loads was evaluated.

This approach was inspired by the specific integration process that was ideated. Its scope was essentially to allow the pre-twist and connection operations, minimizing the needed tools and the forces to be applied. This has a relevant impact both in terms of implementation costs and safety.

Another important aspect is represented by the sensor layout, whose definition, as discussed, was driven by the necessity, from one side, of intensifying the magnitude of the measured strain and, from the other side, of minimizing its impact on twist performance. The role of this system is to support the logic of shape reconstruction even in the presence of multiple load sets and monitor the level of solicitation of the structure during the operative life.

Despite the promising outcomes and the attractive peculiarities, it is worth stressing that the present architecture is not yet suited for real applications. As discussed in [48], some specific aspects should be further matured before arriving at a TRL compliant with an industrial application.

First of all, as already mentioned, even if the stiffness falls within the order of magnitude typical of a real blade structure, only a device with a rigidity of 20% of the real one was considered for safety restrictions. The development of a more rigid structure is compliant with the present architecture since it can be obtained, for example, by just thickening the spars and the ribs. However, to keep the same performance of twist, the authority of the SMA actuators should be increased. Also, in this case, the operation is feasible by, for example, increasing the radius of the cross-section. Moreover, a tubular configuration could be considered to optimize the available room within the blade and ensure the maximum exploitation of the SMA martensite phase. In fact, from one side, the cavity could be exploited to place inside the heating coils, freeing up the outer space while, from the other side, the thickness of the SMA tube could be set to achieve an adequate preload stress level to have full martensite everywhere in the cross-section, different from the current configuration that presents a core of austenite that is not exploitable.

Also, the skin presents margins for improvement. The version considered in this work is in line with the operational conditions simulated in the test facilities, assuring adequate shape maintenance under the external loads and transmitting them to the inner structure. A real application, however, foresees higher solicitation, especially for the centrifugal loads, as discussed in [46]. To reduce any losses in terms of twist transmission and, at the same time, respect the safety requirements, solutions encompassing differential rigidity, that is, compliance around the twist axis and stiff enough towards the other directions, should be considered.

Another critical aspect is the monitoring of the structure in terms of stress level and current shape. As shown, the concept is equipped with inclinometer and strain sensors. Even if these systems can detect the expected solicitations, the development of dedicated logic of shape reconstruction and structural health monitoring would require a more extended network, whose definition would require the assessment of the architecture suited for a real application. A logic of control could handle the signal provided by this network to monitor the stress level and to reconstruct the current configuration of the system, separating the flapping, lagging, and twisting contributions/components. On this basis, it could modulate the heating coils' supply, preventing overheating events.

All these aspects and others will be investigated in future collaborations and investments to enhance the concept's maturation level.

11. Patents

A patent was filed on this topic, entitled "Structural module for fixed and rotary wing", with ID EP21425028.

Author Contributions: Conceptualization, S.A. and A.C.; Methodology, B.G., M.G. and G.B.; Investigation, M.C. and I.D.; Writing—Original Draft Preparation, S.A.; Writing—Review and Editing, S.A. and A.C.; Resources, M.F.M.; Supervision, S.A. and A.C.; Project Administration S.A. All authors have read and agreed to the published version of the manuscript.

Funding: The research was funded by the European Research Council (ERC) under the European Union's Horizon 2020 Research and Innovation Programme as part of the Shape Adaptive Blades for Rotorcraft Efficiency (SABRE) project (Grant Agreement No. 723491).

Institutional Review Board Statement: Not applicable.

Informed Consent Statement: Not applicable.

Data Availability Statement: The data presented in this study are available on request addressed to the corresponding author.

Conflicts of Interest: The authors declare no conflict of interest.

Abbreviations

$_{1,2,3}$	Subscripts referring to the temperatures of the SMA
$_{acc}$	Sensor accuracy
$_{allow}$	Allowable
AoA	Angle of attack
c	Chord
DMU	Digital mock-up
$\Delta\varepsilon$	Strain increase between two different configurations
ε	Strain estimated on the plate integrated with sensors
FEM	Finite Element Model
$_{finish}$	Minimum temperature at which the martensite phase is completely transformed into austenite
h	Convection coefficient

$_{incl}$	Inclinometer
NO_x	Nitrogen oxides
$_{req}$	From requirement
RT	Room temperature
SMA	Shape memory alloy
σ	Stress level in the structure (SMA excluded)
$_{start}$	Temperature at which the martensite phase starts to transform into austenite
T	Temperature
TRL	Technology readiness level
ϑ	Twist transmitted
v	Velocity of the flow
WhT	Whirl tower
WT	Wind tunnel

References

1. ICAO. Effects of Climate Change on Aviation Business and Economics. 2023. Available online: https://www.icao.int/environmental-protection/Documents/Factsheet%20Business%20and%20Economics%20Final.pdf (accessed on 16 September 2023).
2. Aviation Benefits. COVID-19's Impact on Air Transport. 2023. Available online: https://aviaionbenefits.org/covid-19s-impact-on-air-transport/ (accessed on 16 September 2023).
3. ITF. How the War in Ukraine Impacts Aviation—And What to Do about It. 2022. Available online: https://www.itf-oecd.org/war-ukraine-impacts-aviation (accessed on 16 September 2023).
4. Sun, M.; Tian, Y.; Zhang, Y.; Nadeem, M.; Xu, C. Environmental Impact and External Costs Associated with Hub-and-Spoke Network in Air Transport. *Sustainability* **2021**, *13*, 465. [CrossRef]
5. Farhat, K.R.; Rana, A.S. Significant Factors Affecting Quality and Quality Maximizing Methods of Construction Projects In Outskirt Areas of Afghanistan. *IOP Conf. Ser. Earth Environ. Sci.* **2023**, *889*, 012078. Available online: https://iopscience.iop.org/article/10.1088/1755-1315/889/1/012078/pdf (accessed on 16 September 2023). [CrossRef]
6. Moorhouse, D.; Sanders, B.; von Spakovsky, M.; Butt, J. Benefits and Design Challenges of Adaptive Structures for Morphing Aircraft. *Aeronaut. J.* **2006**, *110*, 157–162. Available online: https://www.cambridge.org/core/services/aop-cambridge-core/content/view/D552A6A6BDBD8887EFAD49BF61550512/S0001924000001135a.pdf/benefits-and-design-challenges-of-adaptive-structures-for-morphing-aircraft.pdf (accessed on 16 September 2023). [CrossRef]
7. Clean Aviation. Clean Sky's Morphing Wing Project Brings Shape-Shifting Capabilities to European Regional Aircraft. 2023. Available online: https://www.clean-aviation.eu/media/results-stories/clean-skys-morphing-wing-project-brings-shape-shifting-capabilities-to-european-regional-aircraft (accessed on 16 September 2023).
8. Ozel, C.; Ozbek, E.; Ekici, S. Review on Applications and Effects of Morphing Wing Technology on UAVs. *Int. J. Aviat. Sci. Technol.* **2020**, *1*, 30–40. Available online: https://www.ijast.org/issues/vm01is01/article8.pdf (accessed on 16 September 2023). [CrossRef]
9. The Morphing Wing: Birds Know Best. University of Southern California. Available online: http://illumin.usc.edu/assets/submissions/738/Yap-%20The%20Morphing%20Wing.pdf (accessed on 16 September 2023).
10. WINGS: From the Wright Brothers to the Present. National Air and Space Museum. Available online: https://airandspace.si.edu/stories/editorial/wings-wright-brothers-present (accessed on 16 September 2023).
11. Concilio, A.; Dimino, L.; Lecce, L.; Pecora, R.; Ricci, S. *Morphing Wing Technologies: Large Commercial Aircraft and Civil Helicopters*; Elsevier Butterworth-Heinemann: Oxford, UK, 2017.
12. Ameduri, S.; Concilio, A. Morphing wings review: Aims, challenges, and current open issues of a technology. *Proc. Inst. Mech. Eng. C J. Mech. Eng. Sci.* **2020**, *234*, 4529–4551. [CrossRef]
13. Active Aeroelastic Aircraft Structure (3AS). European Commission. Available online: https://cordis.europa.eu/project/id/G4RD-CT-2002-00679 (accessed on 16 September 2023).
14. Ricci, S.; Scotti, A. Aeroelastic Testing on a Three Surface Airplane. In Proceedings of the 47th AIAA/ASME/ASCE/AHS/ASC Structures, Structural Dynamics, and Materials Conference, Newport, RI, USA, 1–4 May 2006.
15. Integration of Technologies in Support of a Passenger and Environmentally Friendly Helicopter (FRIENDCOPTER). European Commission. Available online: https://cordis.europa.eu/project/id/502773 (accessed on 16 September 2023).
16. Smart High Lift Devices for Next Generation Wings. European Commission. Available online: https://cordis.europa.eu/project/id/213442/reporting (accessed on 16 September 2023).
17. Smart Intelligent Aircraft Structures (SARISTU). Available online: https://cordis.europa.eu/project/id/284562 (accessed on 16 September 2023).
18. Clean Sky. Wikipedia. Available online: https://en.wikipedia.org/wiki/Clean_Sky (accessed on 16 September 2023).
19. Clean Sky 2. Clean Aviation. Available online: https://www.clean-aviation.eu/clean-sky-2 (accessed on 16 September 2023).
20. Clean Aviation. Available online: https://www.clean-aviation.eu/ (accessed on 16 September 2023).

21. JTI-Clean Sky 1-Green Regional Aircraft-Integrated Technology Demonstrator. European Commission. Available online: https://cordis.europa.eu/project/id/999901 (accessed on 16 September 2023).
22. Ameduri, S.; Concilio, A.; Dimino, I.; Pecora, R.; Ricci, S. AIRGREEN2—Clean Sky 2 Programme: Adaptive Wing Technology Maturation, Challenges and Perspectives. In Proceedings of the ASME 2018 Conference on Smart Materials, Adaptive Structures and Intelligent Systems, San Antonio, TX, USA, 10–12 September 2018.
23. Hybrid Electric Regional Wing Integration Novel Green Technologies—HERWINGT. Available online: https://herwingt-project.eu/home (accessed on 16 September 2023).
24. SABRE—Shape Adaptive Blades for Rotorcraft Efficiency. Available online: https://sabreproject.eu/#header (accessed on 16 September 2023).
25. Amoozgar, M.R.; Shaw, A.D.; Zhang, J.; Friswell, M.I. Composite Blade Twist Modification by Using a Moving Mass and Stiffness Tailoring. *AIAA J.* **2019**, *57*, 4218–4225. [CrossRef]
26. Balzarek, C.; Kalow, S.; Riemenschneider, J.; Rivero, A.E. Manufacturing and Testing of a Variable Chord Extension for Helicopter Rotor Blades. *Actuators* **2022**, *11*, 53. [CrossRef]
27. Beaverstock, C.; Woods, B.; Fincham, J.; Friswell, M. Performance Comparison between Optmised Camber and Span for a Morphing Wing. *Aerospace* **2015**, *2*, 524–554. [CrossRef]
28. Zahoor, Y.; Sodja, Y.; De Breuker, R.; Voskuijl, M. Design and Validation of a Passive Camber Morphing Concept for Rotorcraft. In Proceedings of the AIAA SCITECH 2022 Forum, San Diego, CA, USA, 29 December 2021. AIAA 2022-0173.
29. Mail on-line, Science & Tech. Available online: https://www.dailymail.co.uk/sciencetech/article-4301918/Bell-unveils-helicopter-radical-shape-changing-blades.html (accessed on 16 September 2023).
30. Future Helicopters Get SMART. Available online: https://www.nasa.gov/topics/aeronautics/features/smart_rotor.html (accessed on 16 September 2023).
31. DiPalma, M.; Gandhi, F. Autonomous camber morphing of a helicopter rotor blade with temperature change using integrated shape memory alloys. *J. Intell. Mater. Syst. Struct.* **2021**, *32*, 499–515. [CrossRef]
32. Raczyński, R. Structural and dynamic analysis of the prototype main rotor blade section. In Proceedings of the AIP Conference Proceedings, Kazimierz Dolny, Poland, 1–3 September 2021; p. 020031.
33. Hashemi, A.; Jang, J.; Hosseini-Hashemi, S. Smart Active Vibration Control System of a Rotary Structure Using Piezoelectric Materials. *Sensors* **2022**, *22*, 5691. [CrossRef]
34. Wang, X.; Hu, X.; Huang, C.; Zhou, W. Multi-Mode Shape Control of Active Compliant Aerospace Structures Using Anisotropic Piezocomposite Materials in Antisymmetric Bimorph Configuration. *Aerospace* **2022**, *9*, 195. [CrossRef]
35. INWIND—Innovative Wind Conversion Systems (10-20MW) for Offshore Applications. Available online: https://cordis.europa.eu/project/id/308974 (accessed on 16 September 2023).
36. Morphing Blades: New-Concept Tidal Turbine Blades for Unsteady Load Mitigation. Available online: https://voilab.eng.ed.ac.uk/morphing-blades (accessed on 16 September 2023).
37. Goulos, I.; Bonesso, M. Variable Rotor Speed and Active Blade Twist for Civil Rotorcraft: Optimum Scheduling, Mission Analysis, and Environmental Impact. *Aerospace Sci. Technol.* **2019**, *88*, 444–456. [CrossRef]
38. Feszty, D.; Nitzsche, F. Review of Active Rotor Control Research in Canada. *Aerospace* **2018**, *5*, 1. [CrossRef]
39. Van der Wall, B.G.; Rauleder, J.; Abdelmoula, A.; Komp, D.; Kumar, S.; Ondra, V.; Titurus, B.; Woods, B.K.S. Adaptive Twist Rotor Blade Technology: A Review of Recent Developments. *J. Am. Helicopter Soc.* **2019**, *64*, 022001.
40. Polyzos, N.D.; Vouros, S.; Goulos, I.; Pachidis, V. Multi-Disciplinary Optimization of Variable Rotor Speed and Active Blade Twist Rotorcraft: Trade-Off between Noise and Emissions. *Aerosp. Sci. Technol.* **2020**, *107*, 106356. [CrossRef]
41. Kim, D.H.; Hong, S.; Jung, S.N. Multicyclic Vibration Control of a Helicopter Rotor with Active Twist Actuation. *Int. J. Aeronaut. Space Sci.* **2022**, *23*, 303–314. [CrossRef]
42. Bueter, A.; Ehlert, U.C.; Sachau, D.; Breltbach, E. Adaptive Rotor Blade Concepts -Direct Twist and Camber Variation. *J. Intell. Mater. Syst. Struct.* **2004**, *15*, 265–275.
43. Garinis, D.; Dinulovic, M.; Rasuo, B. Dynamic Analysis of Modified Composite Helicopter Blade. *FME Trans.* **2012**, *40*, 63–68.
44. Prouty, R. *Helicopter Aerodynamics Volume I*, 2nd ed.; Eagle Eye Solutions: Guildford, UK; pp. 248–249.
45. Majeti, R.; Stephan, B. Mission-based optimal morphing parameters for rotors with combined chord and twist morphing. *Open Res. Eur.* **2022**, *1*, 121. [CrossRef]
46. Ameduri, S.; Ciminello, M.; Concilio, A.; Dimino, I.; Galasso, B.; Guida, M.; Miceli, M.F.; Riemenschneider, J.; Kalow, S.; Luebker, J.; et al. Whirl Tower Demonstration of an SMA Blade Twist System. *Actuators* **2022**, *11*, 141. [CrossRef]
47. Ameduri, S.; Concilio, A. A shape memory alloy torsion actuator for static blade twist. *J. Intell. Mater Syst. Struct.* **2019**, *30*, 2605–2626. [CrossRef]
48. Miceli, M.F.; Ameduri, S.; Dimino, I.; Pecora, R.; Concilio, A. A Preliminary Technology Readiness Assessment of Morphing Technology Applied to Case Studies. *Biomimetics* **2023**, *8*, 24. [CrossRef] [PubMed]
49. Mehrabi, R.; Taheri Andani, M.; Elahinia, M.; Kadkhodaei, M. Anisotropic Behavior of Superelastic NiTi Shape Memory Alloys; An Experimental Investigation and Constitutive Modeling. *Mech. Mater.* **2014**, *77*, 110–124. [CrossRef]
50. Concilio, A.; Galasso, B.; Ameduri, S. Scaling Effects on Morphing Structures: Preliminary Guidelines for Managing the Effects on a Case Study. *Actuators* **2023**, *12*, 366. [CrossRef]

51. Kuebler. IS40 2-Dimensional Analog Inclinometer. Kuebler.com. 2023. Available online: https://www.kuebler.com/en/products/measurement/inclinometers/product-details/IS40_2-dimensional_analog (accessed on 23 September 2023).
52. Stratasys Ltd. Available online: https://www.stratasys.com/-/media/files/material-spec-sheets/MDS_FDM_ULTEM9085_0919a.pdf (accessed on 23 September 2023).
53. Filoalfa. TDS Alfanylon CF-2020. TDS Alfanylon CF-2020. Version 1.1. Filoalfa. 2020. Available online: https://www.filoalfa3d.com/img/cms/MSDS%20&%20TDS/TDS%20ALFANYLON%20CF-2020.pdf (accessed on 23 September 2023).
54. 7075-T6 Aluminum. Available online: https://asm.matweb.com/search/SpecificMaterial.asp?bassnum=ma7075t6 (accessed on 23 September 2023).
55. AK Steel ARMCO®15-5 PH®VAC CE Product Data Bulletin. Available online: https://www.aksteel.nl/files/downloads/ak_steel_armco%C2%AE_15-5_ph%C2%AE_vac_ce_product_data_bulletin_-feb__2019-_93.pdf (accessed on 23 September 2023).
56. MSC Software Corporation. *Quick Reference Guide*; MSC Software Corporation: Newport Beach, CA, USA, 2015; pp. 2765–2768.
57. XFOIL. Available online: http://web.mit.edu/drela/Public/web/xfoil/ (accessed on 23 September 2023).
58. Convective Heat Transfer. Available online: https://www.engineeringtoolbox.com/convective-heat-transfer-d_430.html (accessed on 23 September 2023).

Disclaimer/Publisher's Note: The statements, opinions and data contained in all publications are solely those of the individual author(s) and contributor(s) and not of MDPI and/or the editor(s). MDPI and/or the editor(s) disclaim responsibility for any injury to people or property resulting from any ideas, methods, instructions or products referred to in the content.